Crust and uppermost mantle beneath the North China Craton, northeastern China, and the Sea of Japan from ambient noise tomography

Yong Zheng[1], Weisen Shen[2], Longquan Zhou[4], Yingjie Yang[1,3], Zujun Xie[1], and Michael H. Ritzwoller[2]

1. State Key Laboratory of Geodesy and Geodynamic, Institute of Geodesy and Geophysics, Chinese Academy of Sciences, Wuhan, Hubei, 430077, China (zhengyong@whigg.ac.cn)
2. Center for Imaging the Earth's Interior, Department of Physics, University of Colorado at Boulder, Boulder, CO 80309-0390 (michael.ritzwoller@colorado.edu)
3. Department of Earth and Planetary Sciences, Macquarie University, 2109 Sydney, Australia (yingjie.yang@mq.edu.au)
4. China Earthquake Network Center, Beijing, 100045, China (lqzhou@seis.ac.cn)

Abstract:

A 3-D shear velocity model of the crust and uppermost mantle to a depth of 100 km is presented beneath the North China Craton (NCC), northeastern China, the Korean Peninsula, and the Sea of Japan. Ambient noise Rayleigh wave tomography is applied to data from more than 300 broad-band seismic stations from Chinese provincial networks (CEArray), the Japanese F-Net, and the IRIS Global Seismic Network, to produce more than 30,000 high quality inter-station measurements across the region. Continuous data from 2007 to 2009 are used to produce group and phase velocity maps from 8 sec to 45 sec period. The model is motivated to constrain the distributed intra-plate volcanism, crustal extension, cratonic rejuvenation, and lithospheric thinning that are hypothesized for the study region. Numerous robust features are observed that impose new constraints on the geometry of these processes, but discussion concentrates only on four. (1) The North-South Gravity Lineament follows the ~40 km contour in crustal thickness, and crustal thickness is anti-correlated with water depth beneath the Sea of Japan, consistent with crustal isostasy for a crust with laterally variable composition. (2) The lithosphere is thin (~70 km) beneath the Songliao-Bohai Graben, but seismically fast. (3) Even thinner more attenuated lithosphere bounds three sides of the eastern NCC (in a horseshoe shape), identifying a region of particularly intense tectonothermal modification where lithospheric rejuvenation may have reached nearly to the base of the crust. (4) Low velocity anomalies reach upward (in a Y-shape) in the mantle beneath the eastern and western borders of the Sea of Japan, extending well into continental East Asia in the west, and are separated by a ~60 km thick lithosphere beneath the central Sea of Japan. This anomaly may reflect relatively shallow slab dehydration in the east and in the west deeper dehydration and convective circulation in the mantle wedge overlying the stagnant slab.

Keywords Ambient noise, surface waves, Sea of Japan, North China Craton, Kyushu microseism

1. Introduction

The goal of this study and companion papers by *Yang et al. [2010, 2011], Zheng et al. [2010b].* and *Zhou et al.* [2011] is to advance toward an integrated, highly resolved shear velocity (Vs) model of the crust and uppermost mantle beneath China. *Zhou et al.* [2011] focus on Southeast China and *Yang et al [2010, 2011]* and *Zheng et al. [2010b]* on western China and Tibet. The complementary focus of the current paper is the Sino-Korean Craton, northeastern China, the Korean Peninsula, and the Sea of Japan. More than 320 seismic stations from Chinese provincial networks in northeastern China and surrounding areas, Japanese F-Net stations [*Okada et al*., 2004], and IRIS GSN stations are the basis for this study (Fig. 1). The resulting station and path coverage that emerges is unprecedented in this region. In order to place strong constraints on crustal structure, ambient noise tomography is employed. As described below, ambient noise tomography has already been employed in other regions of China (e.g., Tibet), at larger scales (e.g., across all of China) at a lower resolution, or in a part of the study region (e.g., North China Platform, Korean peninsula), but a resulting integrated, high-resolution model of the crust and uppermost mantle of the entire region of study has never before been constructed. Such a model is desired to illuminate a set of interconnected tectonic problems that make the Sino-Korean Craton, northeastern China, and the Sea of Japan a particularly fertile area for seismic tomography.

Northeastern China is composed of a mosaic of tectonic blocks and lineated orogenic belts (Fig. 2) that have been arranged and modified by a long, complex, and in some cases enigmatic history of subduction, accretion, and collision dating back to the Archean [e.g., *Sengor and Natal'in*, 1996; *Yin and Nie*, 1996; *Yin, 2010*]. In the south, the wedge-shaped Sino-Korean Craton (SKC), delineated by red lines in Figure 2, is separated from the Yangtze Craton to the south by the Qinling-Dabie-Sulu orogenic belt [*Yin and Nie*, 1993]. The SKC itself consists of the Ordos Block, the North China Platform, Bohai Bay, the Korean Peninsula, as well as marginal and intruding mountain ranges. The Chinese part of the SKC is usually referred to as the North China Craton (NCC) and is divided here into western, central, and eastern parts delineated by red lines. North of

the SKC, the Xing'an-East Mongolia block is separated from the Songliao-Bohai graben by the North-South Gravity Lineament (NSGL). The NSGL extends southward into the SKC near the boundary between the central and eastern parts of the North China Craton. The Songliao-Bohai graben, stretching from the Songliao Basin to the Bohai Gulf, is flanked to the east by the Tancheng-Lujiang (Tanlu) Fault that extends into the SKC and forms the eastern boundary of the North China Craton. The Tanlu Fault also defines the western border of the Northeast Asia Foldbelt [e.g., *Sengor and Natal'in*, 1996; *Yin and Nie*, 1996].

Much of northeastern China has undergone extensive tectonism during the late Mesozoic and Cenozoic eras [e.g.,*Yin*, 2010]. Northeastern China, bounded by the SKC to the south and the Sea of Japan backarc basin to the east, is part of eastern China's Cenozoic volcanic zone [e.g., *Ren et al*., 2002]. Episodic volcanism has been particularly prominent along three volcanic mountain chains (Great Xing'an Range (GXAR), Lesser Xing'an Range (LXAR), Changbai Mountains (CBM). Rifting and extension are believed to have begun in the late Mesozoic [*Tian et al*., 1992] and have led to the development of the Songliao Basin, although the Songliao basement is traced back to the Archean [*Rogers and Santosh*, 2006]. It has also been hypothesized that there is a physical linkage between the sequential openings of the Songliao graben [e.g., *Liu et al.*, 2001] and the Sea of Japan [*Tatsumi et al*., 1989; *Jolivet et al*., 1994]. The SKC formed largely in the Archean, but it is a paradigm of an Archean craton that has lost its lithospheric keel. Petrological and geochemical evidence [e.g., *Menzies et al*., 1993; *Griffin et al*., 1998] suggests that typical cratonic lithosphere existed beneath the entire SKC until at least the Ordovician, after which the SKC was reactivated and lithospheric thinning occurred at the minimum beneath the eastern part of the NCC.

The physical mechanisms that have produced the highly distributed volcanism, crustal extension, cratonic rejuvenation and lithospheric thinning that have occurred across parts of northeastern China remain poorly understood [e.g., *Deng et al*., 2007; *Chen*, 2010]. These issues

86 can be illuminated with seismic images of velocity heterogeneities, internal discontinuities, and
87 crustal and mantle anisotropy, yet the vast majority of the studies to date have been geochemical or
88 petrological in nature. Increasingly, seismological studies are adding new information due in part
89 to the rapid expansion of seismic instrumentation in China over the past few years [e.g., *Zheng et*
90 *al*., 2010a]. These studies include body wave tomography of the mantle [e.g., *Lebedev and Nolet*,
91 2003; *Huang and Zhao*, 2006; *Zhao*, 2009; *Tian et al*., 2009; *Xu and Zhao*, 2009; *Li and van der*
92 *Hilst*, 2010; *Santosh et al*., 2010] and of the crust [e.g., *Sun and Toksoz*, 2006]. Pn tomography [*Li*
93 *et al*., 2011], receiver functions analyses [*Zheng et al*., 2006; *Chen et al*., 2009], and shear wave
94 splitting studies have also been performed [*Zhao et al*., 2008; *Bai et al*., 2010; *Li and Niu*, 2010].
95 Recent body wave results have focused mainly on the eastern part of the NCC, including efforts to
96 image its thin intact lithosphere as well as the potential remnants of the delaminated lithosphere
97 near 400 km depth [e.g., *Chen et al*., 2009; *Xu and Zhao*, 2009].

98 At least parts of northeast China have been imaged by larger scale teleseismic surface wave
99 dispersion studies [e.g., *Ritzwoller and Levshin*, 1998; *Ritzwoller et al*., 1998; *Villaseñor et al*.,
100 2007; *Yanovskaya and Kozhevnikov*, 2003; *Huang et al*., 2003, 2004; *Priestley et al*., 2006].
101 Recent regional scale teleseismic surface wave studies have also been conducted within North
102 China [e.g., *Tang and Chen*, 2008; *Huang et al*., 2009; *Zhou et al*., 2009; *He et al*., 2009; *Pan et al*.,
103 2011], in adjacent regions [e.g., *Yao et al.*, 2006, 2008], and in the Sea of Japan [e.g., *Bourova et al*.,
104 2010; *Yoshizawa et al*, 2010]. Some of these studies are discussed further in the context of our 3D
105 model in section 6.

106 Within the last few years a new method of surface wave tomography has emerged based on
107 using ambient seismic noise to extract surface wave empirical Green's functions (EGFs) and to
108 infer Rayleigh [e.g., *Sabra et al*., 2005; *Shapiro et al*., 2005] and Love wave [e.g., *Lin et al*., 2008]
109 group and phase speeds in continental areas. Compared with traditional earthquake tomography
110 methods, ambient noise tomography is relatively free of artifacts related to the distribution of

earthquakes as well as errors in earthquake locations and source mechanisms. The dominant frequency band for ambient noise tomography lies between about 8 and 40 sec period. Rayleigh waves in this band are sensitive to crustal and uppermost mantle structures. Ambient noise tomography has produced phase and group velocity maps in various regions around the world [e.g., *Moschetti et al*., 2007; *Yang et al*., 2007; *Bensen et al*., 2008] and also is the basis for 3-D crustal and uppermost mantle models of isotropic shear velocity structure [e.g., *Yang et al*., 2008a, 2008b; *Bensen et al*., 2009; *Moschetti et al*., 2010b], radial anisotropy [e.g., *Moschetti et al*., 2010a], and azimuthal anisotropy [e.g., *Lin et al*., 2011]. Ambient noise in east Asia has been shown to be sufficiently well distributed in azimuthal content to be used for surface wave dispersion measurements [e.g., *Yang and Ritzwoller*, 2008] and studies based on ambient noise have been conducted at large scales across all of China [*Zheng et al*., 2008; *Sun et al*., 2010], in regions adjacent to northeastern China [e.g., *Yao et al*., 2006, 2008; *Guo et al*., 2009; *Li et al*., 2009; *Huang et al*., 2010; *Yang et al*., 2010; *Zheng et al*., 2010b; *Zhou et al*., 2011], within the North China Craton [*Fang et al*., 2010], on the Korean Peninsula [*Kang and Shin*, 2006; *Cho et al*., 2007], and in Japan [e.g., *Nishida et al*., 2008].

Ambient noise tomography in northeastern China, the Korean Peninsula, the Sea of Japan, however, is faced with an uncommon technical challenge – the existence of a persistent localized microseismic source on Kyushu Island [*Zeng and Ni*, 2010] in the period band between about 8 and 14 sec, which has been explained to be caused by long period volcanic tremors beneath Aso Volcano in the center of Kyushu [*Kawakatsu et al*., 2011; *Zeng and Ni*, 2011]. This signal causes a significant disturbance that is observable on cross-correlations of ambient noise, which, if left uncorrected, would bias measurements of group and phase velocity in this period band of considerable sensitivity to crustal structure. A principal focus of this paper, therefore, is to identify this disturbance and minimize its effects on the estimated Rayleigh wave group and phase velocity dispersion maps.

136 The present paper is based on Rayleigh wave group and phase velocity maps from 8 to 45 sec
137 period across the Sino-Korea Craton, northeastern China, Korea, and the Sea of Japan. Based on
138 these maps, a 3-D model of the crust and uppermost mantle is constructed by Monte-Carlo
139 inversion along with associated uncertainties. The resulting information complements existing and
140 emerging teleseismic body wave and surface studies by presenting new and much stronger
141 constraints on the structure of the crust and uppermost mantle. The data processing and quality
142 control procedures are described in section 2 and methods used to de-sensitize the data to
143 degradation caused by the persistent, localized Kyushu microseism are presented in section 3. The
144 Rayleigh wave group and phase velocity maps are described in section 4. Section 5 presents a brief
145 discussion of the Monte-Carlo inversion method. Section 6 describes the features of the resulting
146 model. In addition, there is a discussion of several key findings including the relation between sea
147 floor depth and crustal thickness beneath the Sea of Japan, the horseshoe-shape (in map view) of
148 the thinnest lithosphere that bounds the NCC, and the Y-shaped asthenosphere (on vertical profiles)
149 observed beneath the Sea of Japan and the Northeast Asian Foldbelt.

150 **2. Data Processing and Quality Control**

151 The data used in this study are continuous seismic waveforms recorded at broadband stations
152 that existed in and around northeast China and the Sea of Japan from August 2007 to July 2009.
153 Networks providing data include: (1) Chinese Provincial Networks in northeast China consisting
154 of 232 broadband seismic stations (referred to here as CEArray), (2) F-Net in Japan comprising
155 69 long period seismic stations, and (3) the IRIS GSN broadband network in northeast Asia
156 consisting of 22 stations. In total, two years of continuous waveform data have been acquired
157 that were recorded at the 323 stations denoted by solid triangles and squares in Figure 1. Only
158 vertical component data are processed, meaning only Rayleigh waves are studied.

159 The data processing procedures follow those of *Bensen et al*. [2007] and *Lin et al*. [2008].
160 After removing the instrument responses, all records are bandpass filtered between 5 and 150 sec

period. We apply both temporal normalization and spectral whitening. Temporal normalization is applied in an 80 second moving window. Cross-correlations are performed daily between all pairs of stations and then are stacked over the two-year time window. Figure 3a presents example cross-correlation record sections among Chinese stations, among F-Net stations, and inter-station pairs between F-Net stations and Chinese stations.

Data quality control is discussed here and in section 3 and consists of five principal steps, denoted A-E. Most of these steps are based on procedures summarized by *Bensen et al*. [2007] and *Lin et al*. [2008], but because of the mixture of instrument types used in this study and the existence of the Kyushu microseism we add extra steps to ensure the reliability of the resulting dispersion measurements. Step A. A dispersion measurement is retained for a cross-correlation at a given period only if signal-to-noise ratio (SNR) > 15 at that period, where SNR is defined by *Bensen et al*. [2007]. Step B. We remove the effects of the Kyushu microseism, which we discuss further in section 3. Step C. We retain an observation at a given period only if both the group and phase velocities are measured by the automated frequency-time analysis method [*Bensen et al*., 2007]. Group and phase velocity are separate measurements and are not constrained to agree even though they are related theoretically [e.g., *Levshin et al*., 1999]. Step D. We identify and discard stations with bad instrument responses. Step E. This step is broken into two parts. First, we only accept dispersion measurements with path lengths $\geq$ 3 wavelengths. Second, a measurement is retained only if the misfit determined from the final dispersion map is less than 12 sec for group travel time and less than 5 sec for phase travel time, which is somewhat more than twice the standard deviation of the final misfit. Group and phase velocity dispersion measurements of Rayleigh waves are obtained on the symmetric component of inter-station cross-correlations except for paths identified as affected by the Kyushu microseism, as discussed further in section 3.

Because the seismic instruments used in this study differ in origin between China, Japan, and

186 the US, and instruments can vary within CEArray between provinces in China, it is important to
187 identify errors and inconsistencies in response files. For the IRIS network data, F-Net data and
188 most of the Chinese stations, full response (RESP) files including both analog and digital filter
189 stages are available. For a small number of Chinese stations we possess only pole-zero response
190 files missing the digital filtering stages. We find that for the CEArray instruments, the analog
191 pole-zero responses sometimes differ from the full responses computed from the RESP files for
192 stations that have both types of response files. Therefore, we discard the Chinese stations for
193 which we have not been able to acquire RESP files. This affected 36 stations, none of which are
194 included in the 232 Chinese stations shown in Figure 1. Using these response files, all data are
195 converted to velocity prior to cross-correlation.

196 Two other procedures are applied to find other instrument response errors. First, we identify
197 polarity errors (π phase shift) that may represent a units error in the instrument by comparing
198 P-wave first motions observed across the array following deep, distant teleseisms. We also look
199 for half-period misfits based on the final tomography maps at each period. These procedures
200 identified seven stations with polarity errors that are discarded. Second, we compare the phase
201 and group times measured on the positive and negative lags of all cross-correlations, which
202 identifies timing errors as long as both lags have a high SNR [*Lin et al*., 2007]. These procedures
203 identified and discarded three Chinese stations.

204 The 2π phase ambiguity inherent in phase velocity measurements is resolved iteratively, first
205 based on phase velocities predicted by the 3D model of *Shapiro et al*. [2002] and then later on
206 with increasingly refined phase velocity maps that are determined in this study.

207 With more than 300 stations, in principal about 50,000 inter-station cross-correlations could
208 be obtained. Quality control procedures reduce this number appreciably as Table 1 illustrates.
209 After applying the selection criteria, we obtain between ~15,000 to 30,000 group and phase
210 velocity measurements for tomography at periods ranging from 8 to 45 sec, numbers suitable to

produce relatively high-resolution group and phase maps across most of the Sino-Korean Craton, northeastern China, and the Sea of Japan.

3. The Effect of the Localized Persistent Kyushu Microseism

In northeast China, a strong disturbance appears on the cross-correlation waveforms. The record sections shown in Figures 3b and 3c show this disturbance, which appears as precursory signals (identified by white dots) in addition to the expected surface wave part of the empirical Green's function. Another example is presented in Figure 4a, where the disturbance appears at positive correlation lag between 100 and 150 sec, whereas the desired Rayleigh wave signal arrives much later and is seen clearly only at negative correlation lag. The arrival of these disturbances near to the Rayleigh wave wavepackets interferes with the ability to measure Rayleigh wave speeds accurately. In fact, the effect tends to bias Rayleigh waves fast, particularly for Rayleigh wave group velocities.

These precursory signals are due to the persistent, localized Kyushu microseism that has been identified and located by *Zeng and Ni* [2010] on the island of Kyushu, Japan, within our study region. *Kawakatsu et al*. [2011] explain the signal as having originated from long period volcanic tremor beneath Aso Volcano on Kyuhsu Island. The period band of this microseism is dominantly between 8 and 14 sec, and it is somewhat reminiscent of the longer period persistent 26 sec microseism located in the Gulf of Guinea [e.g., *Shapiro et al*., 2006]. We are interested in minimizing its interference with surface wave dispersion measurements across the study region. To do so, we have re-located it, confirming the location of *Zeng and Ni* [2010], and have developed a data processing procedure that allows reliable dispersion curves to be obtained across the Sino-Korean Craton, northeastern China, the Korean peninsula, and the Sea of Japan. The effect of the procedure, however, is to reduce the number of measurements in the region broadly surrounding Kyushu at periods between 10 and 18 sec.

3.1 Re-location of the Kyushu microseism

We use the envelope functions between periods of 10 and 12 sec for the Kyushu signal observed on inter-station cross-correlations to locate the Kyushu microseism. An example envelope function is shown in the bottom panel of Figure 4a. Based on an initial observed group velocity map at 11 sec period, we predict the theoretical arrival time of the Kyushu signal for each inter-station pair for each hypothetical source location on a broad map of the region. We then take the observed amplitude of the envelope function at the predicted time and plot it at the hypothetical source location. An example is shown in Figure 4b, where the hyperbola identifies the set of possible locations for the Kyushu microseism for a particular inter-station pair. We refer to this figure as the migrated envelope function. Finally, we stack over all migrated envelope functions for cross-correlations involving the GSN stations INCN (Inchon, South Korea) and SSE (Shanghai, China), with the paths shown in Figure 4c. The resulting stack of migrated envelope functions is shown in Figure 4d, demonstrating that the re-location of the Kyushu microseism is close to the location from *Zeng and Ni* [2010] (Fig. 4d) on Kyushu Island.

3.2 Eliminating the effect of the Kyushu microseism

Assuming that the Kyushu microseism is a point source, for each inter-station cross-correlation we calculate the expected arrival time of the Kyushu signal as well as the theoretical arrival time of the Rayleigh wave between the two-stations. The relative arrival times of the Kyushu signal (white dots in Fig. 3) and the inter-station Rayleigh waves are highly variable but systematic. When the arrival times of the Kyushu signals are close to the desired surface waves it becomes difficult to separate the signals between 8 and 14 sec period on the symmetric component of the cross-correlations. However, the systematics of the relative arrival times can be exploited to separate the two waves and obtain reliable Rayleigh wave group and phase velocity measurements for most paths by focusing on a single correlation lag. Figure 5 illustrates this point by showing how the Kyushu signal biases group and phase velocity

measurements when the Rayleigh wave and the Kyushu signal arrive nearly simultaneously on the negative lag component of the cross-correlation (Fig. 5a). Figure 5b shows the symmetric component of the cross-correlation. Figure 5c is the positive component of the original cross-correlation, which is free from the Kyushu disturbance. In the frequency-time diagrams [e.g., *Ritzwoller and Levshin*, 1998], large differences between positive and negative correlation lag times are observed at periods shorter than 18 sec, especially in the group velocity dispersion curves. This is illustrated by Figure 5d,e, in which the Kyushu signal disturbs the dispersion curve in Figure 5d but not Figure 5e. The Kyushu signal causes the measured group velocity to bias towards higher velocities (Fig. 5f). At periods longer than 18 sec, however, differences are quite small.

Therefore, to separate the desired inter-station Rayleigh wave from the Kyushu signal we must measure the Rayleigh wave dispersion on the correlation lag opposite from the arrival of the Kyushu signal in the period band of disturbance. The symmetric component, the average of the cross-correlation at positive and negative lag, cannot be used if the Kyushu signal arrives near the inter-station Rayleigh wave at either positive or negative correlation lag time.

In practice, we take the following steps. At periods greater than 18 sec, we ignore the Kyushu disturbance and use the symmetric component for dispersion measurement. At periods less than or equal to 18 sec, the relative arrival time of the Kyushu signal and the surface wave signal at 12 sec period guides the measurement. If the expected apparent speed of the Kyushu signal is greater than 4.5 km/s and the length of the inter-station path is longer than three wavelengths, then the Kyushu signal is well enough separated from the surface wave that phase and group velocities can be measured on the symmetric component. If the expected apparent speed of the Kyushu signal is less than 4.5 km/s, then we make group and phase velocity measurements on the correlation lag opposite from the Kyushu signal.

As Figure 5a exemplifies, the correlation lag on the opposite side of the Kyushu signal may

have a smaller amplitude than the lag containing the Kyushu signal and will have a significantly lower SNR than the symmetric component. Thus, this data processing procedure tends to lower the SNR for many inter-station cross-correlations between 8 and 16 sec period. Because observations are discarded if SNR < 15, this reduces the data set appreciably, as Table 1 shows. We are still left with sufficient high quality measurements to perform tomography across much of the study region, however.

If left untreated, the Kyushu signal would have vitiated our maps predominantly in South Korea, the southern Sea of Japan, and in the Kyushu region from 8 to 14 sec period. Artifacts would have been much stronger on the group velocity than the phase velocity maps. Above 16 sec period, however, even if left untreated, the Kyushu signal would have had only a weak effect on the estimated maps.

4. Rayleigh Wave Dispersion Maps

4.1 Construction of the dispersion maps

Surface wave tomography is applied to the selected dispersion measurements to produce Rayleigh wave group and phase speed maps on a 0.5°×.5° grid using the ray-theoretic method of *Barmin et al*. [2001]. Being mostly determined over regional (non-teleseismic) inter-station distances, the dispersion measurements observed here will not be affected strongly by off-great circle effects [e.g., *Lin et al.*, 2009] except for relatively long paths undergoing a continent-ocean transition. This will primarily affect paths from Japanese F-Net to Chinese stations and the maps of the Sea of Japan may be degraded somewhat by this effect. Finite frequency effects will also be weak in the period band of study [*Lin et al*., 2011]. The tomographic method of *Barmin et al.* is based on minimizing a penalty functional composed of a linear combination of data misfit, model smoothness, and model amplitude. The choice of the damping parameters is based on the optimization of data misfit and the recovery of coherent model features. Due to a shortage of

310 measurements, we are unable to produce reliable maps below 8 sec period and above about 45
311 sec period. The resulting Rayleigh wave dispersion maps, therefore, are constructed between 8
312 and 45 sec on a 2 sec period grid.

313 During tomography, resolution is also estimated via the method described by *Barmin et al*.
314 [2001] with modifications presented by *Levshin et al*. [2005]. Resolution is defined as twice the
315 standard deviation of a 2-D Gaussian fit to the resolution surface at each geographic node.
316 Examples of resolution maps are plotted in Figure 6 for the 16 sec and 35 sec period
317 measurements. Resolution is estimated to be about 100 km across most of the region of study but
318 degrades to 200-400 km near the boundary of our studied area where station coverage is sparse.

319 Histograms of data misfit using the dispersion maps at periods of 14 sec, 20 sec, 30 sec, and
320 40 sec are plotted in Figure 7 for phase and group velocity. Group travel time misfits are
321 typically 3-4 times larger than phase travel time misfits because phase velocity measurements are
322 more accurate [*Bensen et al*. 2007; *Lin et al*., 2008] and group velocity sensitivity kernels have a
323 larger amplitude. The range of standard deviations of the group travel time misfits is 3.97-4.87
324 sec and that of phase travel time is 0.95 - 1.45 sec. Phase travel time misfits of ~1 sec between
325 14 and 30 sec period are indicative of the quality of the data set, being similar to misfits that
326 result from USArray data [e.g., *Lin et al*., 2008].

327 **4.2 Description of the dispersion maps**

328 Group and phase velocity maps at periods of 12, 20, 30, and 40 sec are plotted in Figures 8
329 and 9. Only those areas where the spatial resolution is better than 400 km are shown. The 100 km
330 spatial resolution contour is also plotted as a continuous white line. Because the 3-D model is
331 discussed in considerable detail in section 6, discussion of the dispersion maps here is brief.

332 At each period, the group velocity measurements are sensitive to shallower structures than
333 the phase velocities. Phase velocity maps, therefore, generally should be compared with

somewhat shorter period group velocity maps. Thus, comparison between Figures 8 and 9 reveals that the phase velocity map at 12 sec is similar to the group velocity map at 20 sec and the phase velocity map at 20 sec is quite like the group velocity pattern at 30 sec. Because of the lower uncertainty in the phase velocity measurements, however, the phase velocity maps generally are more accurate than the maps of group velocity.

The dispersion maps are sensitive to quite different structures between short and long periods and between continental and oceanic regions even at the same period. The short period dispersion maps (12 sec group and phase velocity) are primarily sensitive to upper crustal velocities in continental areas, which are dominated by the presence or lack of sediments. In regions with oceanic crust, sensitivity is predominantly to uppermost mantle structure. At intermediate periods (20 sec phase velocity, 20-40 sec group velocity), the maps are mostly sensitive to mid- to lower-crustal velocities beneath continents and continent-ocean crustal thickness variations. At long periods (30-40 sec phase velocity), the maps predominantly reflect crustal thickness variations on the continent and uppermost mantle conditions beneath oceans.

At short periods (12 sec), the dispersion maps in Figures 8-9 exhibit low velocity anomalies where sediments are present [*Bassin et al.*, 2000]; e.g., the Songliao Basin (SLB), Huabei Basin (HB), Bohai Bay (BH), North China Platform (NC), the Yellow Sea (ESYS), and the Tsushima Basin (TB) in the southern Sea of Japan. The younger, Cenozoic age sediments of Bohai Bay and the Huabei Basin of the North China Craton are much slower than the older, largely Mesozoic age sediments of the Songliao Basin. Higher velocities are imaged in the mountains surrounding the basins; e.g, the Great Xing'an Range (GXAR), Lesser Xing'an Range (LXAR), the Changbai Mountains (CBM), the Yinshan Mountains (YSM), and the Taihang Mountains (THM), which is consistent with the presence of crystalline rocks near the surface. Weak positive anomalies are observed in the Korean Peninsula.

At intermediate periods (20 sec phase velocity, 20-30 sec group velocity), relatively low

359 wave speeds are still observed for the deeper basins: Songliao, Huabei, Bohai Bay, and Yellow
360 Sea. Group and phase velocity are very high in the Sea of Japan reflecting oceanic mantle
361 lithospheric shear wave speeds that clearly outline the continental boundary of the oceanic crust.
362 It should be noted that off-great-circle effects that may exist are not severe enough to distort the
363 borders of the oceanic crust badly. A significant low velocity anomaly appears in Xing'an-East
364 Mongolia. The anomaly does not develop along the Tancheng-Lujiang Fault, however, but rather
365 to the west of the Songliao Basin, encompassing the Great Xing'an Range and the Yinshan
366 Mountains north of the Ordos Block. To the east of the NSGL the crust is much thinner than to
367 its west [e.g., *Xu*, 2007].

368 For group velocity at 40 sec and phase velocity at periods of 30-40 sec, four principal
369 observations are worth noting. First, the high wave speed anomalies of the Sea of Japan diminish
370 from 30 sec to 40 sec period on the phase velocity maps. This reflects relatively thin lithosphere
371 beneath the Sea of Japan and increased sensitivity to the underlying asthenosphere by the longer
372 period waves. Second, the Songliao, Huabei, and Bohai basins are situated within the
373 Songliao-Bohai Graben, which is believed to have formed by back-arc extension and potential
374 rifting [*Liu et al.*, 2001]. This graben, extending from the Songliao Basin into Bohai Bay, is
375 associated with a continuous high velocity anomaly, which is clearly observable on the 30 and 40
376 sec phase velocity maps. Third, on the longest period phase velocity maps, low wave speeds are
377 found along the entire length of the Northeast Asia Foldbelt, extending into the Korean Peninsula.
378 Such clear continuous low wave speeds are not apparent on the 40 sec group velocity map
379 because of the shallower sensitivity of group velocities than phase velocities. Apparent
380 discrepancies between phase and group velocities such as this one are reconciled by the 3-D Vsv
381 model, as discussed in section 5. Finally, a belt of low velocities is present on the longest period
382 phase velocity maps in the far eastern Sea of Japan bordering Hokkaido and northern and central
383 Honshu, extinguishing in southern Honshu, and then re-initiating along Kyushu and the Ryukyu
384 Islands.

5. Construction of the 3-D Model

This study is based exclusively on Rayleigh waves, which are primarily sensitive to vertically polarized shear wave speeds (Vsv) that may be slower than horizontally polarized wave speeds (Vsh) in regions where anisotropic minerals are preferentially aligned in the horizontal plane. The velocity difference between Vsv and Vsh is referred to as radial anisotropy. Thus, the model we produce is a Vsv model. In the presence of substantial radial anisotropy, Vsv can be several percent lower than the effective isotropic shear wave speed, Vs. Radial anisotropy is common in both the mantle [e.g., *Ekstrom and Dziewonski*, 1997; *Shapiro and Ritzwoller*, 2002] and the crust [e.g., *Shapiro et al*., 2004; *Moschetti et al*., 2010a,b], and is geographically variable. We will generally refer to our 3D model as being a Vsv model, but for simplicity will also refer to it as a shear wave speed or Vs model.

The 3D Vsv model is based on the Rayleigh wave phase and group speed maps from 8 to 45 sec period on a 0.5°×0.5° grid across the study region. Periods at which resolution is greater than 200 km are not included in the inversion. This determines the outline of the model and in oceanic regions local dispersion curves typically begin at 12 sec period. Local dispersion curves from the eight locations identified with red dots in Figure 2 are shown in Figure 10 with error bars. The group velocity and phase velocity curves shown in Figure 10 are mostly smoothly varying and are able to be fit by a vertically simple Vs model at each point within observational error. In particular, the group and phase velocity curves are reconcilable at each point. Local misfit is presented for each point in Figure 10, where "RMS misfit" means the square root of the reduced chi-square value:

$$\text{RMS misfit} = \left[\frac{1}{N} \sum_i \frac{d_i - p_i}{\sigma_i^2} \right]^{\frac{1}{2}} \quad (1)$$

where d_i is the observed group or phase velocity value, p_i is the value predicted from the model, σ_i is the uncertainty for the observation, and N is the total number of phase plus group velocity values along the dispersion curves.

Uncertainties in the phase velocity curves can be estimated by using the eikonal tomography method [*Lin et al.*, 2009], but the method requires a more uniform array spacing than exists in the study region. Therefore, the uncertainties shown in Figure 10 are not from the data set presented here, but, as discussed in section 2, misfit statistics in the present study are similar to those that emerge in the western US based on the regularly spaced USArray Transportable Array. For this reason, we take the average uncertainties estimated by eikonal tomography using USArray in the western US, but to be conservative we double them [*Lin et al., 2009; Moschetti et al.*, 2010a, 2010b].

The 3D model is constructed via a Monte-Carlo method that is similar to the methods of *Shapiro and Ritzwoller* [2002] and *Yang et al.* [2008] but is more closely related to the method of *Shen et al.* [2011]. Details can be found in *Shen et al.* [2011], which we summarize briefly here.

The starting model for the Monte-Carlo search derives from the Vsv values of the global model of *Shapiro and Ritzwolle*r [2002] with two principal modifications. First, we simplify the starting crustal model considerably: the two sedimentary layers and three crystalline crustal layers of the model of *Shapiro and Ritzwoller* are averaged separately to define only two constant velocity layers (not including a possible water layer). Second, crustal thickness is not allowed to be less than 20 km in the Sea of Japan, as discussed in section 6.1. Uniformly distributed perturbations in Vsv are considered using a single sedimentary layer with variable thickness and shear velocity, four B-splines for Vsv in the crystalline crust, and five B-splines in the mantle to a depth of 150 km, below which the model is a constant velocity half-space. The resulting model is vertically smooth in both the crystalline crust and mantle. Moho depth is allowed to vary in a uniform interval of ± 10 km relative to the starting model. Vsv is constrained to increase

monotonically in the crystalline crust and the depth derivative of velocity directly below Moho is constrained to be positive (i.e., velocity increases with depth right below Moho, but can decrease deeper into the mantle). Both constraints are introduced to reduce the model space, in particular the magnitude of the trade-off between Moho depth with structures at depths adjacent to Moho. The model has no radial anisotropy, thus Vs = Vsh = Vsv. Also, we assume that the crystalline crust and mantle is a Poisson solid and set Vp = 1.73Vs, in the sediments we use Vp = 2.0Vs, and for density we use the scaling relation advocated by *Christensen and Mooney* [1995]: $\rho = 0.541 + 0.3601Vp$, where ρ is in g/cm^3 and Vp is in km/s. We apply a physical dispersion correction [*Kanamori and Anderson, 1977*] using the Q model from PREM [*Dziewonski & Anderson 1981*], and the resulting model is reduced to 1 sec period. Offshore, the water depth is re-calculated based on a 0.2°×0.2° average of bathymetry at each point.

Models are chosen randomly guided by a Metropolis algorithm [e.g., *Mosegaard and Tarantola*, 1995] is accepted if the reduced χ^2 misfit to the dispersion curves is less than twice the minimum misfit, $\chi^2_{\min}$, at each location. Reduced χ^2 misfit is the square of RMS misfit defined in equation (1). RMS misfit averages less than 1.0 across the region of study. Much of the misfit results from group velocities at short periods.

As examples, the procedure yields the eight ensembles of models presented in Figure 11 derived from the eight pairs of Rayleigh wave dispersion curves shown in Figure 10. The ensemble is represented by the grey shaded region, which presents two standard deviations (2σ) around the mean at each depth in each direction. The dispersion curves predicted by the best-fitting model are shown in Figure 10 as the blue (group velocity) and red (phase velocity) lines. At each depth, the Vsv model that we plot in subsequent figures and its uncertainty are defined by the middle and quarter-width (1σ) of the ensemble, respectively. The uncertainties in the model are largest where shear wave speeds trade-off effectively with boundary topography,

456 which occurs near free boundaries in the model: Moho and the base of the sedimentary layer.
457 Thus, uncertainties typically grow near the top of the crystalline crust and both above and below
458 Moho.

459 The eight examples of dispersion curves and the ensembles of models that fit them, presented
460 in Figures 10 and 11, demonstrate how vertically smooth models with two discontinuities can fit
461 the data well across the study region. A closer inspection of the model profiles, however, reveals
462 the limitations of inversion methods based exclusively on surface waves. In particular, the model
463 is affected by the starting model around which the Monte-Carlo method samples, particularly
464 sedimentary thickness and crustal thickness.

465 On the continent, input model-dependence is most important beneath sedimentary basins
466 where our simple parameterization of sedimentary velocities may not faithfully represent local
467 structure. A potential example of this is shown in Figure 11e, beneath the Songliao Basin. Model
468 velocities beneath the basin are very low (~3.2 km/s) in the crystalline upper crust, which causes
469 a large vertical crustal velocity gradient that may not be realistic. Thus, errors in the input model
470 and the simplicity of parameterization of sedimentary structure may bias Vs low in the upper
471 crystalline crust. For this reason, we do not interpret the resulting 3D model at depths above the
472 lower crust. Imposition of constraints from receiver functions [e.g., *Shen et al.*, 2011] would help
473 to resolve this issue, but is beyond the scope of this work.

474 In the ocean, in contrast, crustal thickness in the starting model is more poorly known than on
475 the continent. Surprisingly, however, the resulting model is fairly independent of the starting
476 model. This is illustrated by Figure 12, which shows the resulting ensemble of models for a point
477 in the Sea of Japan with two different starting models in which Moho is at 8 km (Fig. 12a) or 20
478 km (Fig. 12b), respectively. In both cases the surface wave data are fit admirably and nearly
479 identically (e.g., Fig. 11h). With different starting Moho depths of 8 km and 20 km, estimated

480 mantle velocities at 20 km depth are nearly identical in the two ensembles. Crustal velocities and
481 crustal thicknesses differ somewhat (average = 13 km and 15 km, respectively), but are within
482 estimated error. Although crustal thickness may vary from 10 km [*Sato et al*., 2004] to more than
483 20 km [*Kurashimo et al*., 1996] across the Sea of Japan, by setting the starting Moho depth to 20
484 km we are able to estimate mantle velocities reliably and recover crustal velocities and
485 thicknesses to within estimated errors. Further discussion of crustal thickness beneath the Sea of
486 Japan is presented in section 6.2, which describes the observed anti-correlation between crustal
487 thickness and sea floor depth and provides further support for the argument that crustal thickness
488 is relatively well determined beneath the area.

489 Results from the individual vertical profiles are aggregrated into the 3-D model: the middle
490 of the ensemble of accepted models defines the model profile at each point and the spread at
491 each depth yields the uncertainty. Figure 13 shows the Vsv model at four depths: (a) in the lower
492 crust 4 km above Moho, (b) 40 km, (c) 60 km, and (d) 80 km beneath the surface. Because the
493 dispersion curves extend only up to 45 sec period, the model is not reliable beyond a depth of
494 ~100 km. Estimated Moho depth and its uncertainty are shown in Figure 14. Figure 14 also
495 presents the estimated velocity jump across Moho and its uncertainty. Uncertainties in shear
496 wave speed at the four depths shown in Figure 13 are presented in Figure 15. Five vertical slices
497 of the model are presented in Figure 16 along the profiles identified in Figure 14a: A-A'
498 extending northwest-southeast through the Songliao Basin and the Sea of Japan, B-B' running
499 northeast-southwest through the Songliao Basin and the eastern North China Craton, C-C'
500 extending roughly west-east from the Ordos Block through the North China Craton, the Bohai
501 Gulf, Korean Peninsula, and the southern Sea of Japan, D-D' running northwest-southeast from
502 Xing'an-East Mongolia through the Yellow Sea to the East China Sea, and E-E' extending
503 northwest-southeast from the Ordos Block, through the eastern NCC, to the East China Sea. The
504 model is discussed in detail in section 6.

Model uncertainties are presented in Figure 14b for Moho and in Figure 15 corresponding to the horizontal depth slices in Figure 13. Model uncertainties are largest near Moho, i.e., in the lower crust and uppermost mantle as Figure 15a,b reflect. At 40 km depth, large uncertainties follow the NSGL which marks the point at which Moho depth approximately crosses 40 km depth. Uncertainties at 40 km depth are smallest in the Sea of Japan because the crust is thinnest and this depth is most removed from Moho. Uncertainties diminish as one moves deeper beneath Moho, but grow again in the deeper parts of the model as data constraints weaken (Fig. 15c,d). Uncertainties in crustal thickness are nearly homogeneous across the study region, but diminish somewhat beneath the Sea of Japan. Conversely, uncertainties in the velocity jump across Moho are largest beneath the Sea of Japan.

6. Discussion

6.1 Structural features of the 3D model

As discussed in section 5, the trade-off between sedimentary thickness and shear velocities in the upper crust is strong beneath the Songliao and Huabei Basins; thus, we do not present or discuss upper crustal velocities here. Lower crustal velocities are much more robust, however, and they are shown in Figure 13a, which is a profile taken 4 km above Moho. On the continent, lower crustal velocities average about 4.0 km/s, but bifurcate. Velocities are higher, averaging about 4.10 km/s, beneath the Korean peninsula, the Northeast Asian Fold Belt and the Songliao Basin but are slower elsewhere, including the North China Craton, the Xing'an-East Mongolia, and the Yellow Sea, averaging about 3.94 km/s. The high velocity lower crust beneath far eastern Asia and the Songliao Basin may represent compositional differences between these regions and the tectonically distinct North China Craton and Xing'an-East Mongolia. The slowest lower crustal velocities are observed beneath the Sea of Japan, being on average about 3.75 km/s. The lowest velocities occur in the southern part of the basin, which is mainly extended continental

crust [*Tamaki et al., 1992*]. The largest uncertainties in lower crustal velocities are for the Sea of Japan, however (Fig. 15a).

We use the term "mantle lithosphere" here qualitatively and relatively, and it may be substituted with the term "seismic lid". We take it to mean the high velocity zone in the uppermost mantle more of less directly below Moho. Thus, in our usage, the base of the lithosphere is the depth at which velocities begin to decrease beneath higher velocities in the overriding mantle. With this definition, on the vertical profiles in Figure 16 the base of the lithosphere occurs at the depth at which blue colors give way to green colors (~4.5 km/s) if the highest velocities are blues. If the highest velocities are greens (e.g., beneath the Sea of Japan), the base of the lithosphere occurs where the greens give way to white (~4.4 km/s). The term "asthenosphere" is defined more quantitatively, as the region of the mantle where Vs < 4.25 km/s, or where red colors are found in Figure 16. With these definitions, for example, the lithosphere is 70-80 km thick beneath the Songliao Basin (Fig. 16, B-B') and is 50-60 km thick beneath the Sea of Japan (Fig. 16, A-A'). The asthenosphere exists on the vertical profiles only beneath some of the North China Craton (Fig. 16, B-B', C-C'), the regions bordering the Sea of Japan (Fig. 16, A-A', C-C'), and the East China Sea (Fig. 16, D-D', E-E'). Thus, with these definitions, across most of the region the asthenosphere is not reached by 100 km depth. Across most of the region the lithosphere is underlain by a zone that is transitional between lithospheric and asthenospheric, which appears mainly as green and yellow colors on the vertical profiles.

In terms of deeper structures, we describe four principal features: (1) crustal thickness variations across the region, (2) the lithospheric structure of the Songliao – Bohai graben, (3) the uppermost mantle beneath the Sea of Japan and the East China Sea, and (4) the uppermost mantle beneath the North China Craton.

(1) Crustal thickness is presented in Figure 14a. Although internal boundaries such as Moho

553 are notoriously difficult to estimate reliably from surface waves, particularly beneath continents,
554 crustal thickness is seen to reduce below about 40 km along the North-South Gravity Lineament
555 (NSGL). In fact, the NSGL can be seen to mark the approximate location of the 40 km contour in
556 crustal thickness across the region. The region west of the North-South Gravity Lineament
557 (NSGL) is in the crust at 40 km depth, whereas this depth is in the mantle beneath the rest of the
558 region. Thus, the lowest velocities near the western edge of the map in Figure 13b simply reflect
559 crustal wave speeds.

560 Beneath the Sea of Japan, as Figure 12 illustrates, the ability to estimate crustal thickness
561 improves relative to the continent. A blow up of the crustal thickness is presented in Figure 17a.
562 As expected, the crust is thinnest where the sea is deepest, principally in the Japan Basin, which
563 defines the northern and western parts of the Sea of Japan. The crust thickens, for example,
564 beneath the Yamato Rise, the topographic rise in the central Sea of Japan. Crustal thickness
565 beneath the Sea of Japan is discussed further in section 6.2, where the anti-correlation observed
566 between crustal thickness and water depth is used to support the reliability of the crustal
567 thickness estimates in oceanic regions.

568 (2) At 40 km depth east of the NSGL relatively high wave speeds (>4.4 km/s) lie beneath
569 the Songliao Basin and run to the Bohai Sea, as Figure 13b shows. The high velocities beneath
570 the Songliao Basin form a lid that extends to 60-70 km but then terminates, being underlain by
571 more normal continental uppermost mantle wave speeds beneath the Basin by 80 km depth. This
572 can been seen clearly on vertical profiles A-A' and B-B' of Figure 16, in which the relatively
573 thick fast lithosphere beneath the Songliao graben is contrasted with the thinner slower
574 lithosphere of the North China Craton and the Sea of Japan. The mantle lithosphere, however,
575 beneath the Songliao Basin is not cratonic in nature, contrasting with the much thicker
576 lithosphere beneath the Ordos Block (e.g., Fig. 13d). Although the Ordos Block is only partially
577 imaged in this study, high velocities are seen to underlie it in the uppermost mantle extending at

least to 100 km depth (and presumably deeper) as vertical profile C-C' in Figure 16 illustrates. Although the lithosphere underlying the Songliao Basin is not as thin as beneath the North China Craton, it is still thin for a region believed to have a basement of Archean age.

(3) At 40 km depth, relatively high wave speeds (>4.4 km/s) also underlie the Yellow and Japan Seas. Although similar in the uppermost mantle, below 40 km the mantle structures beneath these seas lose their similarity. The uppermost mantle beneath the Yellow Sea is continental in character as profile D-D' in Figure 16 shows. Much lower wave speeds exist in the back-arc spreading region beneath the Sea of Japan, as can been seen on Figure 13c,d. Starting at about 60 km depth, low velocities bound the eastern margin of the Sea of Japan and also to a lesser extent the western margin, extending onto the continent. Low velocities also bound the eastern edge of the East China Sea, east and southeast of the Yellow Sea near the Ryuku Islands. By 80 km depth, the bifurcated low velocity zone across the Sea of Japan has largely merged into a more homogeneous low velocity asthenophere beneath the entire sea, and the western edge of the anomaly has spread further inland to underlie the Northeast Asia Foldbelt, including the volcanic region of the Changbai Mountains. This is presented most clearly in Figure 18, which displays two low velocity contours at 80 km depth: $Vs < 4.25$ km/s and $4.25 \text{ km/s} \leq Vs < 4.35$ km/s. This also can be seen clearly in profile A-A' of Figure 16, which extends across the center of the Sea of Japan, but is also visible in profile C-C' which run through the sea farther south. We refer to the low velocities bounding the Sea of Japan as a "Y-shaped" anomaly on vertical profiles, which is apparent on profile A-A'. A relatively high velocity 50-60 km thick lithosphere is observed beneath the central Sea of Japan, as profiles A-A' and C-C' illustrate. This relatively thin lithosphere should be contrasted with the thicker faster lithosphere beneath the Songliao Basin, which is clearly seen on profile A-A'. The bordering Y-shaped asthenospheric anomaly and the thin lithosphere underlying the Sea of Japan are discussed further in section 6.3.

The East China Sea lies near the southeastern corner of our study region, but like the Sea of

603 Japan its eastern margin near the Ryuku Islands is underlain by low velocities in the uppermost
604 mantle. This is apparent in Figure 18, Figure 13d and vertical profile D-D' in Figure 16. Unlike
605 the Sea of Japan, however, there is no "Y-shaped" anomaly beneath the East China Sea as the
606 western part of the sea merges with fast continental lithosphere beneath the Yellow Sea with no
607 low velocity feature in the uppermost mantle.

608 (4) The North China Craton deviates from most of the rest of continental northern and
609 northeastern China by possessing much slower wave speeds at depths greater than about 60 km.
610 This can be seen clearly on profile B-B' of Figure 16, which shows that the mantle lithosphere
611 beneath the North China craton is thinner and slower than beneath the Songliao Basin. Profile
612 C-C' illustrates, however, that the lithosphere extends deeper than beneath the Sea of Japan, with
613 underlying asthenosphere that is not as slow. However, asthenospheric wave speeds do underlie
614 the lithosphere beneath the North China Craton below about 80 km depth. These low wave
615 speeds in the uppermost mantle are horseshoe in shape on horizontal cross-sections across the
616 eastern North China Craton as seen in Figure 18, in which the low velocities follow the western
617 and eastern flanks of the eastern part of the North China Craton. The middle of the eastern part of
618 the North China Craton is not slow, however. The seismic structure of the North China Craton is
619 discussed further in section 6.4.

620 **6.2 Seafloor depth and crustal thickness beneath the Sea of Japan**

621 The crustal structure beneath the Sea of Japan is highly heterogeneous [e.g., *Taira*, 2001].
622 The Japan Basin is principally oceanic crust, while most of the Yamamoto and Tsushima basins
623 are extended continental crust, the Korean Plateau and Yamamoto Rise are composed mainly of
624 continental crust, and the eastern and southern boundaries of the Sea are rifted continental crust
625 [*Tamaki et al.*,1992]. Thus, crustal thickness varies appreciably across the basin in a way that we
626 expect to be related to seafloor depth, assuming isostatic compensation. Figure 17b presents

seafloor depth (bathymetry) across the Sea of Japan plotted versus solid crustal thickness from our 3-D model. Seafloor depth and our estimate of crustal thickness (Fig. 17a) are correlated, although there is substantial scatter. Assuming that water depth, H_W, is the dependent variable and crustal thickness, H_C, is the independent variable, the least-squares linear fit, shown as the red line in Figure 17b, is $H_W = -0.22\ H_C + 6.07$, where H_W, H_C, and the constant term are in km. The linear fit provides a variance reduction of 57%.

The observed derivative $dH_W/dH_C = -0.22$ provides information about the nature of isostatic compensation in the region. For crustal Airy isostacy, with mantle density equal to 3.32 g/cm^3 and a water density of 1.05 g/cm^3, dH_W/dH_C can be computed for different crustal densities. For an average continental crustal density of ρ_{cont} = 2.75 g/cm^3, $dH_W/dH_C \approx -0.25$, and for an average oceanic crustal density of ρ_{oc} = 2.9 g/cm^3, $dH_W/dH_C \approx -0.19$. Thus, the estimated value of $dH_W/dH_C = -0.22$ is understood to be an average of the values expected if the Sea of Japan were composed homogeneously of either oceanic or continental crust. In fact, much of the scatter around the linear fit seen in Figure 17b is due to crustal heterogeneity across the sea. However, local isostasy may not be dominated by the crystalline crust alone, but may also be affected strongly by sediments and thermal buoyancy from the mantle, both of which have been ignored in the analysis here.

A more careful analysis that considers lateral crustal heterogeneity, thermal buoyancy from the mantle, the effects of sediments, and uncertainties in the crustal thickness estimates is beyond the scope of this paper. The results presented here demonstrate the reliability of the crustal thickness estimates across the Sea of Japan and also provide evidence that further analysis of the relation between seafloor depth and crustal thickness is warranted.

6.3 Lithospheric and asthenospheric structure beneath the Sea of Japan

651 Our 3-D model images what we refer to as a "Y-shaped" anomaly on vertical profiles with
652 low velocity arms reaching upward beneath the eastern and western borders of the Sea of Japan
653 extending well into continental East Asia on the west side (e.g., Fig. 16, A-A'), with an overlying
654 ~60 km thick lithosphere beneath the Sea of Japan. The location of the lowest wave speeds at 80
655 km depth can be seen in Figure 18. In recent years, several other tomographic studies have been
656 performed that are complementary to the ambient noise tomography presented here, which have
657 imaged the mantle beneath the Sea of Japan. These studies possess greater depth penetration
658 although lower resolution than our study and provide validation and assist with interpreting our
659 results.

660 Based on Rayleigh and Love wave phase velocities obtained from teleseismic earthquakes
661 using the two-station method, *Yoshizawa et al.* [2010] present a 3-D model of shear wave speeds
662 from 40 to 200 km depth. Although their resolution is best beneath Japan and fades by the central
663 Sea of Japan, their results in regions of good data coverage are similar to ours in several respects.
664 First, they report an average lithospheric thickness beneath the Yamato Rise and the Japan Basin
665 of 60 ±10 km, which is similar to what we observe (e.g., Fig. 16, A-A', C'C'). Second, they also
666 observe low velocity anomalies at 75 km depth bordering Honshu beneath the eastern Sea of
667 Japan and the East China Sea, west of the Ryuku Islands. Thus, they also image the eastern arm
668 of the Y-shaped anomaly that we report here and, like our model, observe it to migrate westward
669 with depth. Their data coverage does not extend into east Asia. However, the teleseismic body
670 wave study of *Zhao et al.* [2007] presented a large-scale image of the upper mantle beneath east
671 Asia, which shows the stagnation of the subducted Pacific Plate beneath the Sea of Japan and
672 clear low velocity anomalies in the back-arc region. This study concentrates interpretation on the
673 release of volatiles from the slab at several depths to produce the low velocity anomalies
674 observed in the back-arc region.

675 Thus, *Yoshizawa et al.* [2010] serves to validate our model and *Zhao et al.* [2007] provides a

means to interpret the Y-shaped anomaly based on what they call the "Big Mantle Wedge" model of the Japanese back-arc and the devolatilization of the subducted slab. In their interpretation, the western arm of the Y-shaped anomaly beneath the western Sea of Japan and the East Asian Fold Belt would be caused by dehydration reactions of the stagnant slab in the mantle boundary layer (410-660 km). These warm hydrated upwellings are the cause of volcanism in East Asia (e.g., Changbai volcano) and may have precipitated the crustal rifting that led to the opening of the Sea of Japan. Presumably, the stagnant slab would generate hydrated plumes across the entire Sea of Japan, but the stretched and thinned continental lithosphere remains intact beneath the central Sea of Japan, as Figure 16 A-A', C-C' demonstrate, impeding upward migration of the hydrated plumes. These plumes would then become part of a westward directed convecting system that would amplify mantle hydration in the western Sea of Japan, near the rift margin. The eastern arm of the Y-shaped anomaly would be caused by slab dehydration at shallower depths, possibly caused by antigorite-related reactions. Thus, the Y-shaped anomaly reflects the details of shallow and deep slab dehydration and convective circulation in the mantle wedge above a stagnant slab.

6.4 Lithospheric Rejuvenation of the North China Craton

The Chinese part of the Sino-Korean Craton, called the North China Craton (NCC), is composed of two Archean blocks, the eastern and the western NCC, which are separated by the central NCC. The central NCC is a Paleoproterozoic orogen called the Trans-North China Orogen. The three parts of the NCC are enclosed by red lines in Figure 2. The NCC is believed to have cratonized by about 1.85 Ga, but the eastern NCC has undergone significant tectonothermal rejuvenation from the Ordovician to Cenozoic [*Menzies at al., 1993, 2007; Griffin et al., 1998; Gao et al., 2002, 2004; Zhao et al., 2005, 2008*]. These conclusions have been based on basalt-borne xenoliths and geophysical evidence for thin lithosphere (< 100 km) with high heat flow in this region from the early Cenozoic to the present [e.g., *Menzies et al., 1993; Griffin et al., 1998; Fan et al., 2000; Xu, 2001; Wu et al., 2005; Chen et al., 2006, 2008, 2009*]. Most studies

agree that the central and western parts of the NCC have evolved differently than the eastern NCC during Phanerozoic time [e.g., *Xu et al., 2004; Xu, 2007*], although some recent seismic studies point to localized lithospheric thinning in the central and even western NCC [e.g., *Huang et al., 2009; Chen et al., 2009*] and the generally high lateral heterogeneity of the lithosphere underlying the NCC. The mechanism of Phanerozoic lithospheric rejuvenation and its variability across the NCC remain intensely debated [e.g., *Chen, 2010* for a recent summary]. Understanding of the Phanerozoic lithospheric tectonics would be improved with clearer images of the current structure of the crust, mantle lithosphere, and asthenosphere across the NCC.

To this debate our 3-D model presents new relatively high-resolution images of the crust and uppermost mantle beneath most of the NCC. Crustal velocities beneath the eastern NCC are not particularly distinct from surrounding regions (e.g., Fig. 13a), although the crust may be slightly thinner, on average (Fig. 14a). More significantly, the eastern NCC hosts a "horseshoe" shaped anomaly in map view in the uppermost mantle, which is identified at 80 km depth in Figure 13d and, perhaps more clearly, by the blue contour in Figure 18. The velocities are lowest in the northern part of the North China Platform near the intersection of the NSGL with the boundary between the central and eastern NCC. The low velocities continue southward, flanking the eastern NCC along the NSGL in the west and the TLF in the east. Low velocities also extend into small parts of the central NCC and the western NCC near the Datong Volcanoes. The south central part of the NCC is not particularly slow in the uppermost mantle as Figure 16 profile E-E' illustrates, which reveals the considerable variability of lithospheric structure even within the eastern NCC.

Within the "horseshoe" shaped anomaly bounding three sides of the eastern NCC (Fig. 18), the lithosphere can be seen to be about 60 km thick on vertical profiles B-B' and C-C' of Figure 16. The flanks of the eastern NCC are underlain by asthenospheric low velocity anomalies below 70 km depth as can be seen on profiles B-B', C-C', and E-E'. Profile B-B' illustrates that the lithosphere is not simply thin; the velocities are lower than beneath the Songliao Basin to the north

726 and the Ordos Block to the west. Thus, we hypothesize that the low velocity anomalies that bound
727 three sides of the eastern NCC identify a region of more intense tectonothermal activity than in
728 south-central part of the eastern NCC. Indeed, lithospheric rejuvenation may have reached nearly
729 to the base of the crust in the most intensely altered zones.

730 **7. Conclusions**

731 This paper presents a high-resolution 3-D shear velocity model of the crust and uppermost
732 mantle with associated uncertainties across the North China Craton, northeastern China, the
733 Korean Peninsula, and the Sea of Japan constructed from the dispersion characteristics of
734 Rayleigh waves obtained from ambient noise cross-correlations. Broadband stations from
735 Chinese Provincial Networks, the Japanese F-Net, and the IRIS GSN have produced two-year
736 continuous time series from 2007 into 2009 that form the basis for these results. Phase and group
737 velocity maps from 8 sec to 45 sec period are first constructed, which constrain earth structures
738 in the crust and uppermost mantle to a depth of about 100 km. The dispersion maps are
739 geologically coherent, displaying the signatures of sedimentary basins, mountain roots,
740 ocean-continent variations, and anomalies due to rifting and volcanism. The maps at different
741 periods and between phase and group velocities are consistent with one another, and vertically
742 relatively smooth Vsv models fit the observations.

743 To generate the dispersion maps presented here, the effects of the persistent localized
744 Kyushsu microseism had to be eliminated in the dispersion measurements. We present a method
745 based on locating the microseism (thereby confirming the location of *Zeng and Ni* [2010]),
746 predicting the arrival of the disturbing signal on the ambient noise cross-correlations, and
747 obtaining the dispersion measurements by using the Green's functions at the opposite
748 cross-correlation lag times for the station pairs in which the apparent speed of the Kyushu signal
749 is less than 4.5km/s.

750 Ambient noise tomography places unique constraints on the structure of the crust and

uppermost mantle, providing information complementary to body wave travel times, receiver functions, longer period teleseismic surface waves, gravity, and other types of data. The motivation for the 3-D model is to produce new constraints on the volcanism, crustal extension, cratonic rejuvenation, and lithospheric thinning that are hypothesized for the region of study. The model presented here provides new information about these processes, particularly about the geometry (the geographic distribution and depth extent) of the observed features in the top 100 km. A detailed interpretation of the model is inconsistent with the scope of this paper, but we focus discussion on four principal model features: crustal thickness variations, particularly those associated with the North-South Gravity Lineament and beneath the Sea of Japan, the prominent but thin lithosphere underlying the Songliao-Bohai Graben, the "Y-shaped" mantle low velocity anomaly (on vertical profiles) bordering the Sea of Japan, and a "horse-shoe" shaped asthenospheric anomaly (in map view) bounding three sides of the eastern North China Craton.

(1) The NSGL is observed to follow approximately the 40 km crustal thickness contour. Beneath the Sea of Japan, crustal thickness is anti-correlated with water depth, and the relationship is consistent with expectations based on crustal isostasy for a laterally compositionally variable crust. (2) The Songliao-Bohai Graben is underlain by a high velocity lower crust and a fast mantle lithosphere that extends to about 70 km depth. The lithosphere is not attenuated, that is seismic velocities are high, but it is thinner than expected for a region with parts traceable back to the Archean. (3) Low velocity anomalies reach upward beneath the eastern and western borders of the Sea of Japan, extending well into continental East Asia on the west side. The arms of this Y-shaped anomaly are separated by the intervening overlying lithosphere, which is ~60 km thick and may represent stretched continental lithosphere. We argue that the Y-shaped structure in the east reflects relatively shallow slab dehydration and in the west deeper dehydration and convective circulation in the mantle wedge overlying the stagnant slab. (4) Very thin, attenuated lithosphere bounds three sides of the eastern North China Craton (NCC), but somewhat thicker faster lithosphere underlies the central and southern parts of the eastern

NCC. These low velocity anomalies identify a region of intense tectonothermal modification where lithospheric rejuvenation may have reached nearly to the base of the crust.

In the future, assimilating similar results from a companion paper for southern China [*Zhou et al*., 2011] will allow the 3-D model to extend across all of eastern China. The geometry of the observing array makes the application of differential travel time methods for earthquakes difficult, such as eikonal tomography [*Lin et al*., 2009], Helmholtz tomography [*Lin and Ritzwoller*, 2011], or two-plane wave tomography [e.g., *Yang et al*., 2008b]. However, the success of such methods would allow dispersion maps to be extended to longer periods and, therefore, for the model to reach greater depths in the mantle. In addition to the production of a 3-D Vs model of the crust and uppermost mantle, other research envisioned includes the estimation of azimuthal anisotropy, which would place complementary constraints on the physical processes that motive this study. In addition, future understanding of the dispersion characteristics of Love waves would allow estimation of radial anisotropy, which reflects deformation undergone by the crust and uppermost mantle.

Acknowledgement. The authors wish to thank An Yin and an anonymous reviewer for constructive criticism of an early draft of this paper and Fan-Chi Lin and Shijie Zhong for valuable conversations. This work was done while the first author visited the University of Colorado at Boulder over a period of one year. The work was supported by CEA grant 201008007, CAS grant kzcx2-yw-142 and Y009021002, NSFC grant (40974034, 41174086), US NSF-EAR award 0944022, and US NSF-OISE sub-award 0730154. Most of the waveform data for this study were provided by the Data Management Centre of the China National Seismic Network at the Institute of Geophysics, China Earthquake Administration and F-Net in Japan. In addition, the facilities of the IRIS Data Management System were used to access data required in this study. The IRIS DMS is funded through the US National Science Foundation under Cooperative Agreement EAR-0552316.

References

Bai, L., H. Kawakatsu, and Y. Morita (2010), Two anisotropic layers in central orogenic belt of the North China Craton, Tectonophysics, 494:138-148.

Barmin, M. P., M. H. Ritzwoller, and A. L. Levshin (2001), A fast and reliable method for surface wave tomography, *Pure Appl. Geophs*., 158:1351-1375.

Bassin, C., G. Laske, and G. Masters (2000), The current limits of resolution for surface wave tomography in North America. *EOS Trans AGU 81,* F897.

Bensen, G. D., M. H. Ritzwoller, M. P. Barmin, A. L. Levshin, F. Lin, M. P. Moschetti, N. M. Shapiro, and Y. Yang (2007), Processing seismic ambient noise data to obtain reliable broad-band surface wave dispersion measurements, *Geophys. J. Int.*, 169: 1239-1260.

Bensen, G.D., M.H. Ritzwoller, and N.M. Shapiro (2008), Broad-band ambient noise surface wave tomography across the United States, *J. Geophys. Res.*, 113, B05306, 21 pages, doi:10.1029/2007JB005248, 2008.

Bensen, G. D., M. H. Ritzwoller and Y. Yang (2009), A 3-D shear velocity model of the crust and uppermost mantle beneath the United States from ambient seismic noise, *Geophys. J. Int.*, 177: 1177-1196.

Bourova, E., K. Yoshizawa, and K. Yomogida (2010). Upper mantle structure of marginal seas and subduction zones in northeastern Eurasia from Rayleigh wave tomography, *Phys. Earth. Planet. Int.*, 183: 20-32.

Chen, L. (2010). Concordant structural variations from the surface to the base of the upper mantle in the North China Craton and its tectonic implications, *Lithos*, 120: 96-115.

Chen, L., T. Zheng, W. Xu (2006). Athinned lithospheric image of the Tanlu Fault Zone, eastern China: constructed from wave equation based receiver function migration, *J. Geophys. Res.*, 111, B09312. doi:10.1029/2005JB003974.

Chen, L., T. Wang, L. Zhao, T. Zheng (2008). Distinct lateral variation of lithospheric thickness in the Northeastern North China Craton, *Earth Planet. Sci. Lett.*, 267: 56–68.

Chen, L., C. Cheng, and Z. Wei (2009), Seismic evidence for significant lateral variations in lithospheric thickness beneath the central and western North China Craton, *Earth Planet. Sci. Lett.,* 286: 171-183.

Cho, K.H., Herrmann, R.B., Ammon, C.J., Lee, K. (2007), Imaging the upper crust of the Korean Peninsula by surface-wave tomography. *Bull. Seism. Soc. Am.,* **97** (1): 198-207 Part B Sp. Iss. S.

Christensen, N.I. & Mooney, W.D. (1995), Seismic velocity structure and composition of the continental crust: A global view*, J. Geophys. Res.,*100(B6): 9761–9788.

Deng, J., S. Su, Y. Niu, C. Liu. G. Zhao, X. Zhao, S. Zhou, and Z. Wu (2007), A possible model for the lithospheric thinning of the North China Craton: Evidence from the Yanshanian (Jura-Cretaceous) magmatism and tectonism, *Lithos*, 96: 22-35.

858 Dziewonski, A. and D. Anderson (1981), Preliminary reference Earth model, *Phys. Earth Planet.*
859 *Int.,* 25(4): 297–356.
860 Ekstrom, G., and A. M. Dziewonski (1997), Three-dimensional velocity structure of the Earth's
861 upper mantle, in Upper Mantle Heterogeneities From Active and Passive Seismology,
862 edited by K. Fuchs, pp. 187–198, Kluwer Acad., Norwell, Mass.

863 Fan,W., H. Zhang, J. Baker, K. Jarvis, P.R.D. Mason, M. Menzies (2000). On and off the North China
864 Craton: where is the Archaean keel?, *Journal of Petrology*, 41(7):933–950.

865 Fang L., J. Wu, Z.Ding, G. Panza (2010), High resolution Rayleigh wave group velocity tomography in
866 North-China from ambient seismic noise, *Geophys. J. Int.*, 181(2): 1171-1182.

867 Gao, S., R. Rudnick, R. Carlson, W. McDonough, Y. Liu (2002), Re–Os evidence for replacement of
868 ancient mantle lithosphere beneath the North China Craton, *Earth Planet. Sci. Lett.*, 198: 307–322.

869 Gao, S. R.L. Rudnick, H. Yuan, X. Liu, Y. Liu, W. Xu, W. Ling, J. Ayers, X. Wang, and Q. Wang (2004),
870 Recycling lower continental crust in the North China craton, *Nature*, 432:892-897.

871 Gao, S. R.L. Rudnick, W. Xu, H. Yuan, Y. Liu, R. Walker, I. Puchtel, X. Liu, H. Huang, X. Wang, J. Yang
872 (2008), Recycling deep cratonic lithosphere and generation of intraplate magmatism in the North China
873 Craton, *Earth Planet. Sci. Lett.,* 270: 41-53.

874 Griffin, W.L., A. Zhang, S.Y. O'Reilly, C. Ryan (1998), Phanerozoic evolution of the lithosphere beneath the
875 Sino-Korean Craton. In: Flower, M., S. Chung, C. Lo, T. Lee (Eds.), *Mantle dynamics and plate*
876 *interactions in East Asia*, AGU Geodynamics Series, Vol. 27: 107-126.

877 Guo, Z., X. Gao, H. Yao, J. Li, W. Wang (2009), Mid-crustal low velocity layer beneath the central Himalaya
878 and southern Tibet revealed by ambient noise array tomography, *Geochem. Geophys. Geosyst.,* 10(5),
879 Q05007, doi:10.1029/2009GC002458.

880 He, Z., T. Ye, and Z. Ding (2009), Surface wave tomography for the phase velocity in the northeastern part of
881 North China, *Chinese J. Geophys*., 52(5): 1233-1242.

882 Huang, H., H. Yao, and R.D. van der Hilst (2010), Radial anisotropy in the crust of SE Tibet and SW China
883 from ambient noise interferometry, *Geophys. Res. Lett.,* 37, L21310, 5 pp., doi:10.1029/2010GL044981.

884 Huang, J. and D. Zhao (2006), High-resolution mantle tomography of China and surrounding regions*, J.*
885 *Geophys. Res.*, 111, doi:10.1029/2005JB004066.

886 Huang, Z., H. Li, Y. Zheng, and Y. Peng (2009), The lithosphere of North China Craton from surface wave
887 tomography, *Earth Planet. Sci. Lett.,* 288:164-173.

888 Huang, Z., Y. Peng, Y. Luo, Y. Zheng, W. Su (2004), Azimuthal anisotropy of Rayleigh waves in East Asia.
889 *Geophys. Res. Lett*. 31, L15617. doi:10.1029/2004GL020399.

890 Huang, Z., W. Su, Y. Peng, Y. Zheng, and H. Li (2003), Rayleigh wave tomography of China and adjacent

891 regions, *J. Geophys. Res.*, 108, doi:10.1029/2001JB001696.

892 Jolivet, L. K., K. Tamaki, M. Fournier (1994), Japan Sea, opening history and mechanism: a synthesis. *J.*
893 *Geophys. Res*. 99:22237-22259.

894 Kang, T.S. and Shin, J.S. (2006), Surface-wave tomography from ambient seismic noise of accelerograph
895 networks in southern Korea. *Geophys. Res. Lett.* **33** (17), L17303.

896 Kanamori, H. and D. Anderson (1977), Importance of physical dispersion in surface wave and free oscillation
897 problems : Review, *Revs. Geophys. Space Phys*., 15(1):105-112.

898 Kawakatsu, H., M. Yamamoto, S. Kaneshima, and T. Ohkura (2011), Comment on "A persistent localzed
899 microseismic source near the Kyushu Island, Japan" by Xiangfang Zeng and Sidao Ni, *Geophys. Res.*
900 *Lett.,* in press.

901 Kurashimo, E., Shinohara, M., Suyehiro, K., Kasahara, J., Hirata, N. (1996), Seismic evidence for stretched
902 continental crust in the Japan Sea. *Geophys. Res. Lett.* 23:3067-3070.

903 Lebedev, S., and G. Nolet (2003), Upper mantle beneath Southeast Asia from S velocity tomography, *J.*
904 *Geophys. Res.*, 108, doi:10.1029/2000JB000073.

905 Levshin, A., M.H. Ritzwoller, and J. Resovsky (1999), Source effects on surface wave group travel times and
906 group velocity maps, *Phys. Earth Planet. Int.*, 115:293 - 312.

907 Levshin, A., M. Barmin, M.H. Ritzwoller, and J. Trampert (2005), Minor-arc and major-arc global surface
908 wave diffraction tomography, *Phys. Earth Planet. Ints.*, 149:205-223.

909 Li, C. and R.D. van der Hilst (2010), Structure of the upper mantle and transition zone beneath Southeast Asia
910 from traveltime tomography, *J. Geophys. Res.*, 115, B07308, doi:1029/2009JB006882.

911 Li, H.Y., W. Su, , C.Y.Wang, , Z. X. Huang (2009), Ambient noise Rayleigh wave tomography in western
912 Sichuan and eastern Tibet. *Earth Planet. Sci. Lett*. 282 (1-4): 201-211.

913 Li, J. and F. Niu (2010), Seismic anisotropy and mantle flow beneath northeast China inferred from regional
914 seismic networks, *J. Geophys. Res*., 115, B12327, doi:10.1029/2010JB007470.

915 Li, Z., T. Hao, and Y. Xu (2011), Uppermost mantle structure of the North China Craton: Constraints from
916 interstation Pn travel time diference tomography, *Chin. Sci. Bull.,* 56:1691-1699.

917 Lin, F.C., M.P. Moschetti, and M.H. Ritzwoller (2008), Surface wave tomography of the western United States
918 from ambient seismic noise: Rayleigh and Love wave phase velocity maps, *Geophys. J. Int.*,
919 doi:10.1111/j1365-246X.2008.03720.x.

920 Lin, F.C. and M.H. Ritzwoller (2011), Helmholtz surface wave tomography for isotropic and azimuthally
921 anisotropic structure, *Geophys. J. Int.*, in press.

922 Lin, F., M.H. Ritzwoller, J. Townend, M. Savage, S. Bannister (2007). Ambient noise Rayleigh wave

923 tomography of New Zealand, *Geophys. J. Int.*, 170(2): 649-666, doi:10.1111/j.1365-246X.2007.03414.x,

924 Lin, F., M.H. Ritzwoller, and R. Snieder (2009), Eikonal tomography: Surface wave tomography by
925 phase-front tracking across a regional broad-band seismic array, *Geophys. J. Int.*, 177(3): 1091-1110.

926 Lin, F., M.H. Ritzwoller, Y. Yang, M. Moschetti, and M. Fouch (2011), Complex and variable crustal and
927 uppermost mantle seismic anisotropy in the western United States, *Nature Geoscience*, 4(1): 55-61.

928 Liu, J., J. Han, and W. Fyfe (2001), Cenozoic episodic volcanism and continental rifting in Northeast China
929 and possible link to Japan Sea development as revealed from K-Ar geochronology, *Tectonophysics*,
930 339:385-401.

931 Menzies, M.A.,W. Fan, and M. Zhang (1993), Paleozoic and Cenozoic lithoprobes and the loss of >120 km of
932 Archean lithosphere, Sino-Korean craton, *China. Geol. Soc. Long. Spec. Pub.*, 76:71-81.

933 Menzies, M., Y. Xu, H. Zhang, and W. Fan (2007), An integration of geology, geophysics, and geochemistry: A
934 key to understanding the North China Craton, *Lithos*, 96: 1-21.

935 Moschetti, M., M.H. Ritzwoller, and F. Lin (2010a), Seismic evidence for widespread crustal deformation
936 caused by extension in the western USA, *Nature*, 464(7290): 885-889.

937 Moschetti, M., M.H. Ritzwoller, F. Lin, and Y. Yang (2010b), Crustal shear velocity structure of the western
938 US inferred from ambient noise and earthquake data, *J. Geophys. Res.*, 115, B10306,
939 doi:10.1029/2010JB007448.

940 Moschetti, M., M. Ritzwoller, and N. Shapiro (2007), Surface wave tomography of the western United States
941 from ambient seismic noise: Rayleigh wave group velocity maps, *Geochem. Geophys. Geosyst.*, 8,
942 Q08010, doi:10.1029/2007GC001655.

943 Mosegaard, K., and A. Tarantola (1995) , Monte Carlo Sampling of Solutions to Inverse Problems, *J. Geophys.*
944 *Res.,* 100(B7): 12431-12447.

945 Nishida, K., Kawakatsu, H., Obara, K. (2008), Three-dimensional crustal S wave velocity structure in Japan
946 using microseismic data recorded by Hi-net tiltmeters. *J. Geophys. Res.-Solid Earth,* **113** (B10):B10302.

947 Okada, Y., K. Kasahara, S. Hori, K. Obara, S. Sekiguchi, H. Fujiwara, and A. Yamamoto (2004), Recent
948 progress of seismic observation networks in Japan – Hi-net, F-net, K-Net and KiK-net, *Earth Planets*
949 *Space*, 56, xv-xxviii.

950 Pan, J., Q. Wu, Y. Li, F. Zhang, G.. Zhang (2011), Rayleigh wave tomography of the phase velocity in North
951 China, *Chinese J. Geophys*., 54(1): 67-76.

952 Priestley, K., E. Debayle, D. McKenzie, S. Pilidou (2006), Upper mantle structure of eastern Asia from
953 multimode surface waveform tomography. *J. Geophys. Res*. 111, B10304. doi:10.1029/2005JB004082.

954 Ren, J. K. Tamaki, S. Li, and J. Zhang (2002). Late Mesozoic and Cenozoic rifting and its dynamic setting in
955 eastern China and adjacent seas, *Tectonophysics*, 344: 175-205.

956 Ritzwoller, M.H. and A. Levshin (1998), Eurasian surface wave tomography: Group velocities, *J. Geophys.*
957 *Res.*, 103: 4839-4878.

958 Ritzwoller, M.H., A. Levshin, L. Ratnikova, and A. Egorkin (1998), Intermediate period group velocity maps
959 across Central Asia, Western China, and parts of the Middle East, *Geophys. J. Int.*, 134: 315-328.

960 Rogers, J.J.W. and M. Santosh (2006), The Sino-Korean Craton and supercontinent history: Problems and
961 perspectives, *Gondwana Res.,* 9:21-23.

962 Sabra, K. G., P. Gerstoft, P. Roux, W. A. Kuperman, and M. C. Fehler (2005), Surface wave tomography from
963 microseisms in Southern California, *Geophys. Res. Lett.* 32, L14311.

964 Santosh, M., D. Zhao, and T. Kusky (2010), Mantle dynamics of the Paleoproterozoic North China Craton: A
965 perspective based on seismic tomography, *J. Geodyn*. 49: 39-53.

966 Sato, T., Shinohara, M., Karp, B.Y., Kulinich, R.G., Isezaki, N. (2004), P-wave velocity structure in the
967 northern part of the central Japan Basin, Japan Sea with ocean bottom seismometers and airguns. *Earth*
968 *Planets Space,* 56: 501–510.

969 Sengor, A.M. C., B. A. Natal'in (1996), Paleotectonics of Asia: fragments of a synthesis. In *The tectonic*
970 *evolution of Asia*, edited by Yin, A. and Harrison, T. M., Cambridge University Press, pp. 486-640.

971 Shapiro, N.M. and M.H. Ritzwoller (2002), Monte-Carlo inversion for a global shear velocity model of the
972 crust and upper mantle, *Geophys. J. Int.*, 151: 88-105.

973 Shapiro, N.M., M. Campillo, L. Stehly, and M.H. Ritzwoller(2005), High-resolution surface wave tomography
974 from ambient seismic noise. *Science* 307, 1615-1618.

975 Shapiro, N.M., M.H. Ritzwoller, and G.D. Bensen (2006), Source location of the 26 sec microseism from cross
976 correlations of ambient seismic noise, *Geophys. Res. Lett.*, 33, L18310, doi:10.1029/2006GL027010.

977 Shapiro, N.M., M.H. Ritzwoller, P. Molnar, and V. Levin (2004). Thinning and flow of Tibetan crust
978 constrained by seismic anisotropy, *Science*, 305: 233-236.

979 Shen, W., M. H. Ritzwoller, and V. Schulte-Pelkum (2011), Joint inversion of surface wave dispersion and
980 receiver functions: A Monte-Carlo approach., in preparation.

981 Sun, Y. and N. Toksoz (2006), Crustal structure of China and surrounding regions from P wave travetime
982 tomography, *J. Geophys. Res.,* 111, B03310, doi:10.1029/2005JB003962.

983 Sun, X., X. Song, S. Zheng, Y. Yang, M. Ritzwoller (2010), Three dimensional shear velocity structure of crust
984 and upper mantle in China from ambient noise surface wave tomography, *Earthquake Science*,
985 23:449-463, doi:10.1007/s11589-010-0744-3.

986 Taira, A. (2001), Tectonic evolution of the Japanese island arc system. *Annu. Rev. Earth Planet. Sci*,
987 29:109-134.

988 Tamaki, K., K. Suychiro, J. Allan, J.C. Ingle, Jr., K.A. Pisciotto (1992). Tectonic synthesis and implications of
989 Japan Sea ODP Drilling, *Proc. Ocean Drilling Pgm, Scientific Results*, Vol. 127/128, Pt. 2, 1333-1348.

990 Tang, Q. and Chen, L. (2008), Structure of the crust and uppermost mantle of the Yanshan Belt and adjacent
991 regions at the northeastern boundary of the North China Craton from Rayleigh wave dispersion analysis.
992 *Tectonophysics* 455: 43–52.

993 Tatsumi, Y., Y. Otofuji, T. Matsuda, and S. Nohda (1989), Opening of the Sea of Japan back-arc basin by
994 asthenospheric injection, *Tectonophysics*, 166: 317-329.

995 Tian, A.Y., P. Han, and K.D. Xu (1992), The Mesozoic-Cenozoic east China rift system, *Tectonophysics*,
996 208:341-363.

997 Tian, Y., Zhao, D., Sun, R., Teng, J. (2009), Seismic imaging of the crust and upper mantle beneath the North
998 China Craton, *Phys. Earth Planet. Int*., 172: 169–182.

999 Villaseñor, A., Y. Yang, M. H. Ritzwoller, and J. Gallart (2007), Ambient noise surface wave tomography of
1000 the Iberian Peninsula: Implications for shallow seismic structure, *Geophys. Res. Lett.*, 34, L11304,
1001 doi:10.1029/2007GL030164.

1002 Wu, F., J. Lin, A. Simon, X. Zhang, J. Yang (2005). Nature and significance of the Early Cretaceous giant
1003 igneous event in eastern China. *Earth and Planet. Sci. Lett.*, 233:103–119.

1004 Xu, Y.(2001). Thermotectonic destruction of the Archean lithospheric keel beneath eastern China:
1005 evidence, timing, and mechanism. *Physics and Chemistry of the Earth* A, 26: 747–757.

1006 Xu, Y. (2007), Diachronous lithospheric thinning of the North China Craton and formation of the
1007 Daxin'anling-Taihangshan gravity lineament, *Lithos*, 96: 281-298.

1008 Xu, P. and D. Zhao (2009), Upper-mantle velocity structure beneath the North China Craton: implications for
1009 lithospheric thinning, *Geophys. J. Int.*, 177: 1279-1283.

1010 Xu, Y.G., Chung, S.L., Ma, J.L., Shi, L.B. (2004). Contrasting Cenozoic lithospheric evolution and
1011 architecture in the eastern and western Sino-Korean craton: constraints from geochemistry of basalts
1012 and mantle xenoliths. *Journal of Geology*, 112: 593–605.

1013 Yang, Y., M. Ritzwoller. A. Levshin, and N. Shapiro (2007), Ambient noise Rayleigh wave tomography across
1014 Europe. *Geophys. J. Int*., 168: 259-274.

1015 Yang, Y., and M. Ritzwoller (2008). Characteristics of ambient seismic noise as a source for surface wave
1016 tomography. *Geochem. Geophys. Geosyst.*, 9, Q02008, doi:10.1029/2007GC001814.

1017 Yang, Y., A. Li, and M. Ritzwoller (2008a). Crustal and uppermost mantle structure in southern Africa revealed
1018 from ambient noise and teleseismic tomography. *Geophysi. J. Int.,* 174: 235-248.

1019 Yang, Y., M. Ritzwoller, F.. Lin, M. Moschetti, and N. Shapiro (2008b), Structure of the crust and uppermost
1020 mantle beneath the western United States revealed by ambient noise and earthquake tomography, *J.*
1021 *Geophys. Res.*, 113, B12310, doi:10.1029/2008JB005833.

1022 Yang, Y., Y. Zheng, J. Chen, S. Shou, S. Celyan, E. Sandvol, F. Rilmann, K. Priestley, T.M. Hearn, J.F. Ni, L.D.
1023 Brown, and M.H. Ritzwoller (2010), Rayleigh wave phase velocity maps of Tibet and the surrounding
1024 regions from ambient seismic noise tomography, *Geochem., Geophys., Geosys.*, 11(8), Q08010,
1025 doi:10.1029/2010GC003119.

1026 Yang, Y., M.H. Ritzwoller, Y. Zheng, A. Levshin, and Z. Xie (2011), A synoptic view of the distribution and
1027 connectivity of the mid-crustal low velocity zone beneath Tibet. Submitted to *J. Geophys. Res.*

1028 Yanovskaya, T.B., Kozhevnikov, V.M. (2003). 3D S-wave velocity pattern in the upper mantle beneath the
1029 continent of Asia from Rayleigh wave data. *Phys. Earth Planet. Int.* 138: 263–278.

1030 Yao, H., R. D. van der Hilst, and M. V. de Hoop (2006), Surface-wave array tomography in SE Tibet from
1031 ambient seismic noise and two-station analysis—I. Phase velocity maps, *Geophys. J. Int.,* 166: 732–744,
1032 doi:10.1111/j.1365-246X.2006.03028.x.

1033 Yao, H., C. Beghein, and R. D. van der Hilst (2008), Surface wave array tomography in SE Tibet from ambient
1034 seismic noise and two-station analysis—II. Crustal and upper-mantle structure, *Geophys. J. Int.*, 173:
1035 205–219, doi:10.1111/j.1365-246X.2007.03696.x.

1036 Yin, A. (2010), Cenozoic tectonic evolution of Asia: A preliminary synthesis, *Tectonophysics*, 488, 293-325.

1037 Yin, A., and S. Nie (1993), An indentation model for the North and South China collision and the development
1038 of the Tan-Lu and Honam Fault Systems, eastern Asia, *Tectonics*, 12(4):801-813,
1039 doi:10.1029/93TC00313.

1040 Yin, A., and S. Nie (1996), A Phanerozoic palinspastic reconstruction of Chinaand its neighboring regions, in
1041 *The Tectonic Evolution of Asia*, edited by A. Yin and T. M. Harrison, Cambridge Univ. Press, New York,
1042 pp. 442-285.

1043 Yoshizawa, K., K. Miyake, and K. Yomogida (2010), 3D upper mantle structure beneath Japan and its
1044 surrounding region from inter-station measurements of surface waves, *Phys. Earth Planet. Int.,*
1045 183:4-19.

1046 Zeng, X, and S. Ni (2010), A persistent localized microseismic source near the Kyushu Island, Japan, *Geophys.*
1047 *Res. Lett.*, 37, L24307, doi:10.1029/2010GL045774.

1048 Zeng, X, and S. Ni (2011), Correction to "A persistent localized microseismic source near the Kyushu Island,

Japan". *Geophys. Res. Lett.*, 38, L16320, doi:10.1029/2011GL048822.

Zhang, P., Q. Deng, G. Zhang, J. Ma, W. Gan, W. Min, F. Mao, and Q. Wang (2003), Active tectonic blocks and strong earthquake in the continent of China. *Science in China D Series*, 46(s): 13-24.

Zhao, D. (2009), Multiscale seismic tomography and mantle dynamics. *Gondwana Research*, 15: 297–323.

Zhao, D., S. Maruyama, and S. Omori (2007). Mantle dynamics of Western Pacific and East Asia: Insight from seismic tomography and mineral physics, *Gond. Res.*, 11:120-131.

Zhao, G.C., Sun, M.,Wilde, S.A., Li, S.Z. (2005). Late Archean to Paleoproterozoic evolution of the North China Craton: key issues revisited. *Precambrian Res.*, 136: 177–202.

Zhao, L. T. Zheng, and G. Lu (2008), Insight into craton evolution: Constraints from shear wave splitting in the North China Craton, *Phys. Earth Planet. Int.,* 168:153-162.

Zheng, S., X. Sun, X. Song, Y. Yang, and M.H. Ritzwoller (2008), Surface wave tomography of China from ambient seismic noise, *Geochem. Geophys. Geosyst.*, 9, Q0502, doi:10.1029/2008GC001981.

Zheng, T., L. Chen, L. Zhao, W. Xu, and R. Zhu (2006), Crust–mantle structure difference across the gravity gradient zone in North China Craton: Seismic image of the thinned continental crust, *Phys. Earth Planet. Int.,* 159: 43-58.

Zheng, X. F., Z. X. Yao, J. H. Liang, and J. Zheng (2010a), The role played and opportunities provided by IGP DMC of China National Seismic Network in Wenchuan earthquake disaster relief and researches, *Bull. Seismol. Soc. Am*., 100(5B): 2866-2872.

Zheng, Y., Y. Yang, M.H. Ritzwoller, X. Zheng, X. Xiong, Z. Li (2010b), Crustal structure of the northeastern Tibetan Plateau, the Ordos Block, and the Sichuan Basin from ambient noise tomography, *Earthquake Science*, 3:465-476, doi:10.1007/s11589-010-0745-3.

Zhou, L., J. Xie, W. Shen, Y. Zheng, Y. Yang, H. Shi, and M.H. Ritzwoller (2011), Ambient noise surface wave tomography of South China, submitted to *Geophys. J. Int.*.

Zhou, R.M., B.W. Stump, R.B. Herrmann, Z. X. Yang, and Y. T. Chen (2009), Teleseismic receiver function and surface-wave study of velocity structure beneath the Yanqing-Huailai Basin Northwest of Beijing, *Bull. Seism. Soc. Am.*, 99(3):1937-1952.

Table 1: Number of measurements retained after each step in data quality control.

Period (s)	Step A	Step B	Step C	Step D	Step E (phase)	Step E(group)
12	27033	20732	20701	19365	17887	16873
14	31356	25770	25740	24082	22606	21593
20	33573	33573	33564	31555	29835	30250
25	28990	28990	28982	27398	25561	25878
30	25495	25495	25491	24210	22258	22148
35	21976	21976	21972	20985	18991	18663
40	18172	18172	18165	17488	15432	14984
45	14503	14503	14495	14031	11991	11575

Figure Captions

Figure 1. The broadband seismic stations used in this study. The blue triangles are the Chinese provincial broadband seismic stations (CEArray), the red triangles are the F-Net long period stations and the red squares are other broadband stations, mostly from the IRIS GSN. The black box defines the study region.

Figure 2. The geological setting of this study. Red lines mark the boundaries of the Sino-Korean Craton (SKC), the solid white line identifies the North South Gravity Lineament (NSGL), the dashed black line is the Tancheng-Lujiang fault (TLF), and black lines outline blocks and tectonic boundaries (Zhang, et al., 2003). The North China Craton is the part of the SKC in China, and is sub-divided by red lines into western, central, and eastern parts. Feature names are abbreviated as follows: PS: Phillipine Sea Plate, OK; Okhotsk Plate, NCP: North China Platform, YB: Yangtze Block, SLB: Songliao Basin, JB: Japan Basin; TB: Yamato Basin, TB: Tsushima Basin, SB: Sichuan Basin, OR: Ordos Block, BH: Bohai Bay, GXAR: Great Xing'an Range, LXAR: Lesser Xing'an Range, CBM: Changbai Mountain Range, YSM: Yinshan Mountain Range, ESYS: East Shandong Yellow Sea Block, NEFB: Northeast Asian Fold Belt, and HB: Huabei Basin. Red dots with letters mark locations of the dispersion curves and 1D shear velocity profiles shown in Figs. 10 and 11.

Figure 3. Record sections of cross-correlations obtained from two years of waveform data (a) between Chinese provincial network stations, (b) between F-Net stations, and (c) between the Chinese stations and F-Net stations. The white dots identify the expected arrival times for the Kyushu persistent microseism.

Figure 4. Process to locate the Kyushu microseism. (a) Top Panel: raw cross-correlation (CC) between station SSE and INCN (blue triangles in (b)). Bottom Panel: The envelope function of the CC filtered between 10 and 12 sec period. The Kyushu microseismic signal arrives at ~130 sec. (b) The migrated hyperbola from the envelope function in (a), normalized so its maximum value is 1. (c) Paths used to locate the Kyushu microseism are plotted with black lines. We use all paths associated with stations SSE and INCN (yellow triangles). (d) Stack of migrated hyperbolas to locate the Kyushu microseism. Blue circle is the location of *Zeng and Ni* (2010).

Figure 5. Cross-correlations and corresponding frequency-time diagrams illustrating the effect of the persistent Kyushu microseism. (a) Cross-correlation between stations HXQ of CEArray and STM of F-Net, where the expected arrival time of the signal from the Kyushu microseism (marked "Kyushu") is close to the arrival time of the surface wave (marked "Surface") on the negative lag component. (b) Example waveform disturbed by

the Kyushu microseism: symmetric component cross-correlation in which the positive and negative components in (a) are averaged. (c) Example waveform undisturbed by the Kyushu microseism: positive component of the cross-correlation in (a). (d) & (e) Frequency-time (group velocity) diagrams from (b) and (c), respectively. (f) Comparison between the group velocity curves of cross-correlations shown in (b) and (c). Red triangles and stars are the phase and the group velocity curves from disturbed signal. Blue symbols show the group and phase velocity curves of the undisturbed signal.

Figure 6. Resolution estimates at periods of 16 and 35 sec, presented in units of km and defined as twice the standard deviation of a 2-D Gaussian fit to the resolution surface at each geographic node (*Barmin et al., 2001*). The black box shows the region of study.

Figure 7. Misfit histograms at periods 14, 20, 30, and 40 sec, respectively. The top figures show the group velocity misfit and the lower figures are the phase velocity misfits. The standard deviations are shown on each panel.

Figure 8. Group velocity maps at periods of 12, 20, 30, and 40 sec. Group velocities are plotted as perturbations relative to the average velocity (U_0) within the 400 km resolution contour and the thick white line is the 100 km resolution contour. Other lines show tectonic and geological boundaries identified in Fig. 2.

Figure 9. Same as Fig. 8, but for phase velocity maps at periods of 12, 20, 30 and 40 sec.

Figure 10. Phase (red lines) and group (blue lines) velocity curves at the eight locations identified with letters in Fig. 2. The dispersion curves are predicted by the center of the ensemble of models shown in Fig. 11 for each location. The RMS misfits are calculated by equation (1).

Figure 11. Shear wave (V_{sv}) velocity profiles at the eight selected locations identified with letters in Fig. 2 constructed to fit the corresponding dispersion curves shown in Fig. 10. The gray corridor is the 2σ (st dev) uncertainty and the dashed lines indicates crustal thickness.

Figure 12. Comparison between inversions performed in the Sea of Japan (point H, Fig. 2) using data from Fig. 10h with two starting models identified with blue lines: (a) Moho at 8 km and (b) Moho at 20 km. The resulting ensembles of models are quite similar, with differences within model uncertainties.

Figure 13. Four horizontal depth slices through the 3-D Vsv model: (a) in the lower crust 4 km above Moho, (b) 40 km, (c) 60 km, and (d) 80 km depth. Color bars beneath each panel give the range of shear wave speeds in km/s.

Figure 14. (a) Estimated crustal thickness and (b) 1σ uncertainty in crustal thickness, both in km.

The lines A-A', B-B', etc. in (a) are the location of the vertical profiles shown in Fig. 16. (c) Shear velocity jump across Moho (km/s) and (d) 1σ uncertainty in the shear velocity jump across Moho, also in km/s.

Figure 15. Uncertainty (1σ) in Vsv at the four depths shown in Fig. 13. Uncertainties are in km/s.

Figure 16. Four vertical profiles through the 3-D model along the lines shown in Fig. 14a. Crustal velocities are presented using an absolute scale and mantle velocities are defined relative to 4.35 km/s.

Figure 17. (a) Blow-up of part of Fig. 14a, showing crustal thickness across the Sea of Japan (in km). Contours of bathymetry are over-plotted in increments of 1 km to illustrate the anti-correlation between crustal thickness and seafloor depth. (b) Plot of seafloor depth versus solid crustal thickness (crustal thickness minus ocean depth) with values on a 0.5°×0.5° grid across the Sea of Japan shown as blue dots. The red line is the least-squares fit line.

Figure 18. Simplified representation of the 3D model, showing the distribution of low velocities at 80 km depth with two contours: red: Vsv ≤ 4.25 km/sec, blue: 4.25 < Vsv ≤ 4.35 km/s. The red contour identifies the "Y-shaped" anomaly that underlies the Sea of Japan and parts of northeastern Asia believed to arise from slab dehydration at several depths overlying the stagnant slab. The blue region surrounding the red contour is the large area of the uppermost mantle affected by back-arc spreading. The blue contour within the North China Craton identifies the "horseshoe" shaped anomaly that flanks the eastern North China Craton, believed to result from intense tectonothermal modification that may have reached as high as the base of the crust.

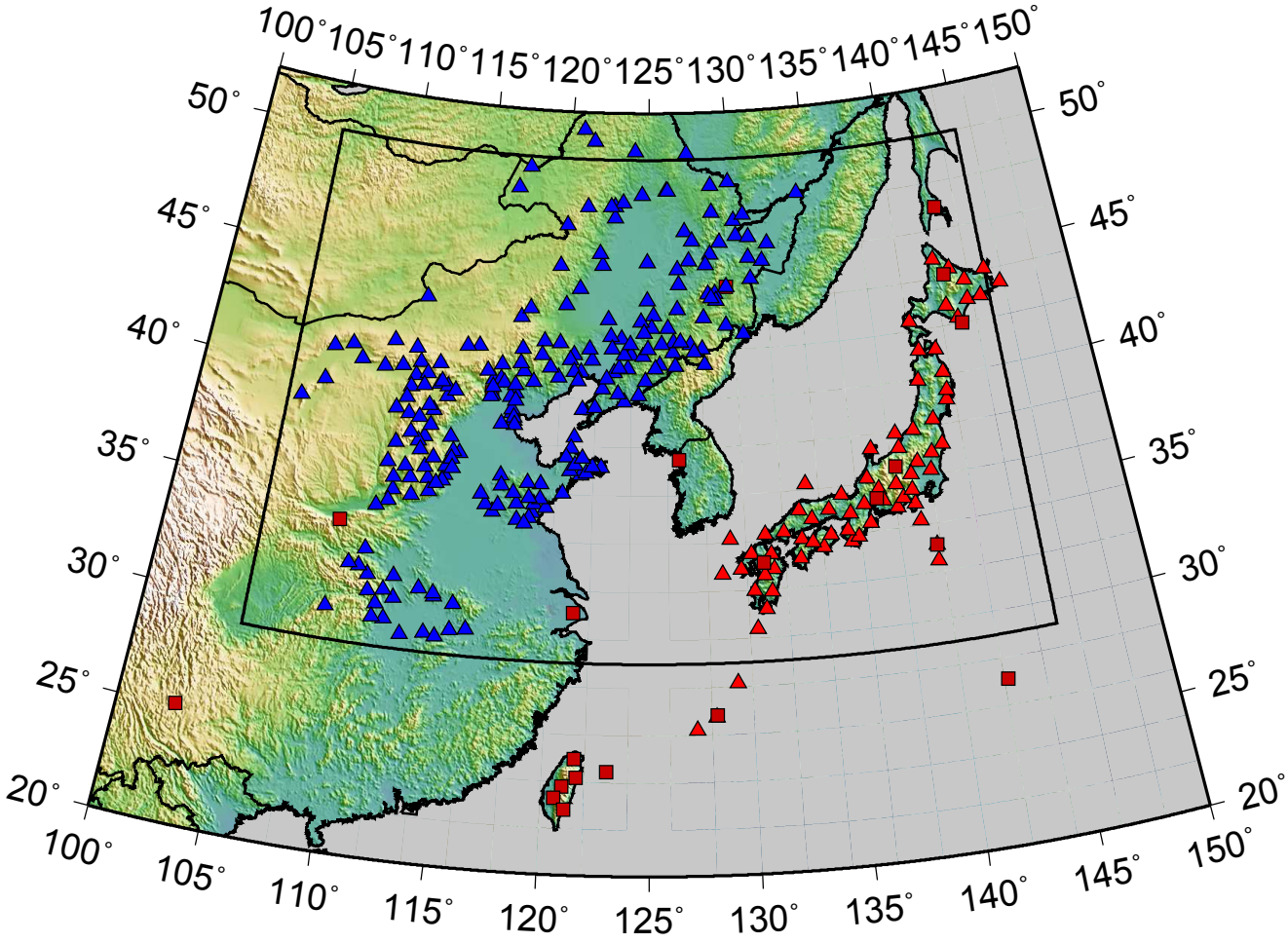
100°
105°
110°
115°
120°
125°
130°
135°
140°
145°
150°
50°
45°
40°
35°
30°
25°
20°

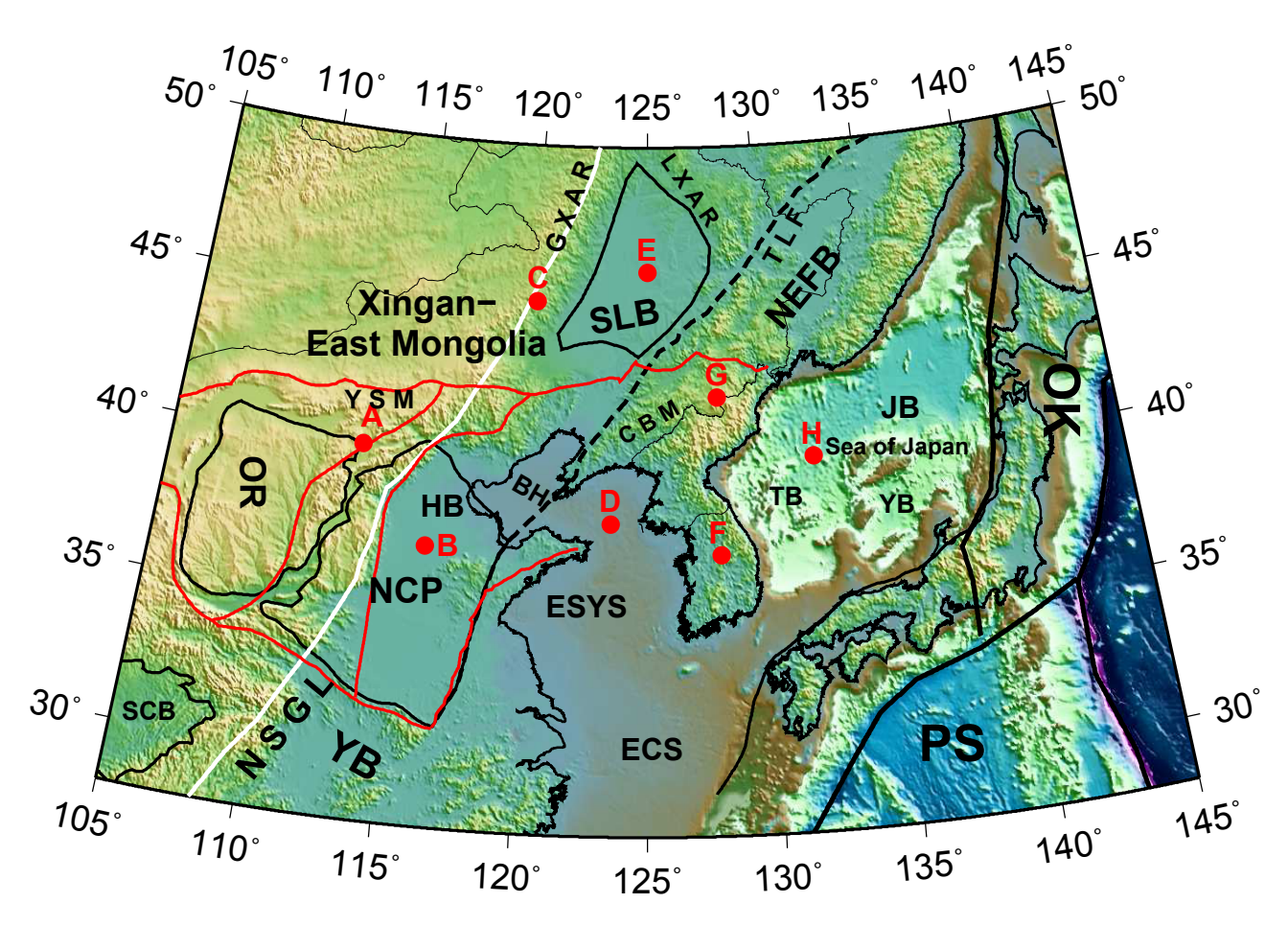
105°
110°
115°
120°
125°
130°
135°
140°
145°
50°
45°
40°
35°
30°
GXAR
LXAR
TLF
NEFB
SLB
Xingan–
East Mongolia
C
E
G
YSM
A
OR
CBM
JB
H
Sea of Japan
OK
BH
HB
B
D
TB
YB
F
NCP
ESYS
SCB
NSGL
YB
ECS
PS

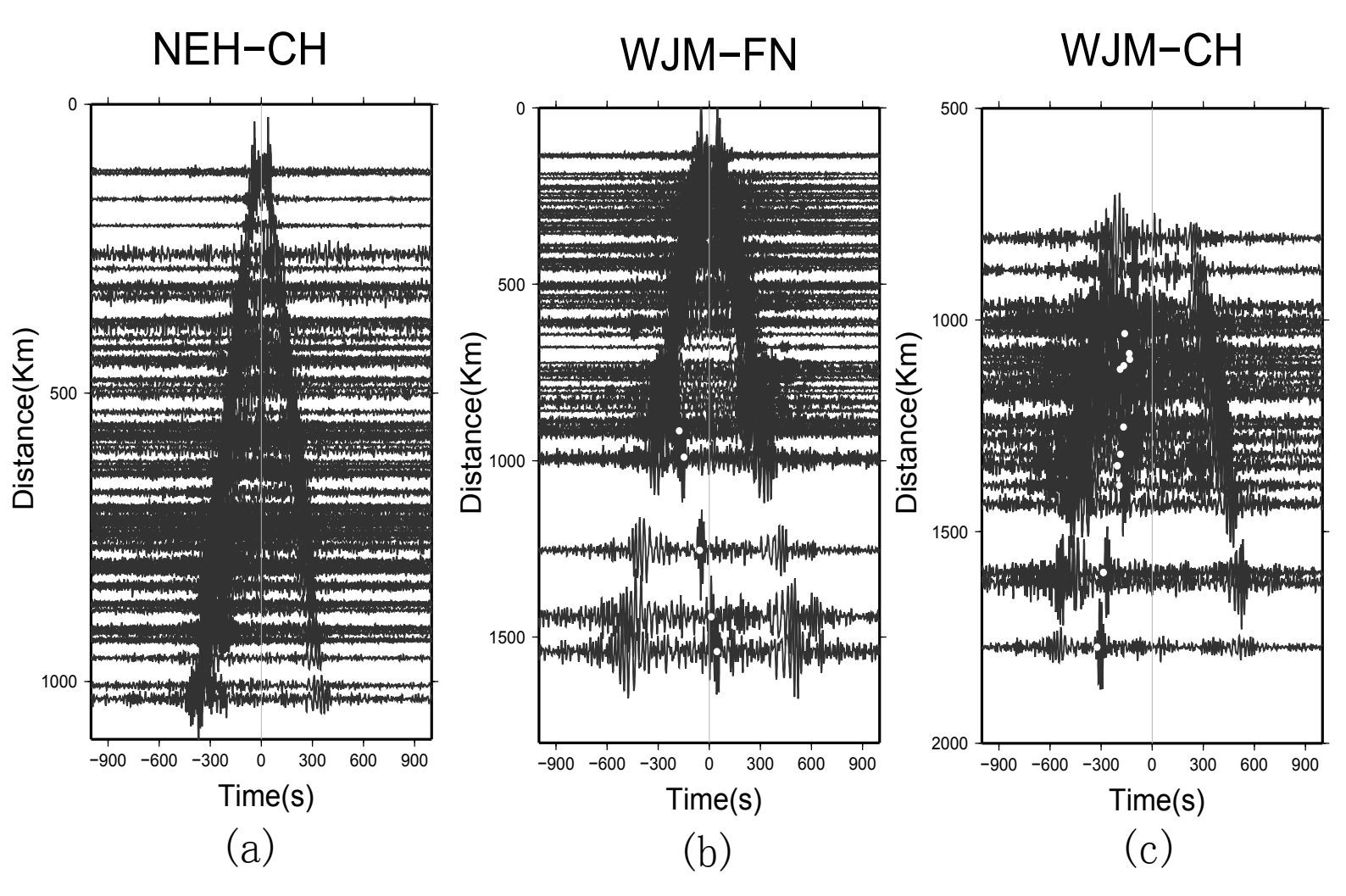
NEH-CH
WJM-FN
WJM-CH
Distance(Km)
Time(s)
0
500
1000
1500
2000
-900
-600
-300
300
600
900
(a)
(b)
(c)

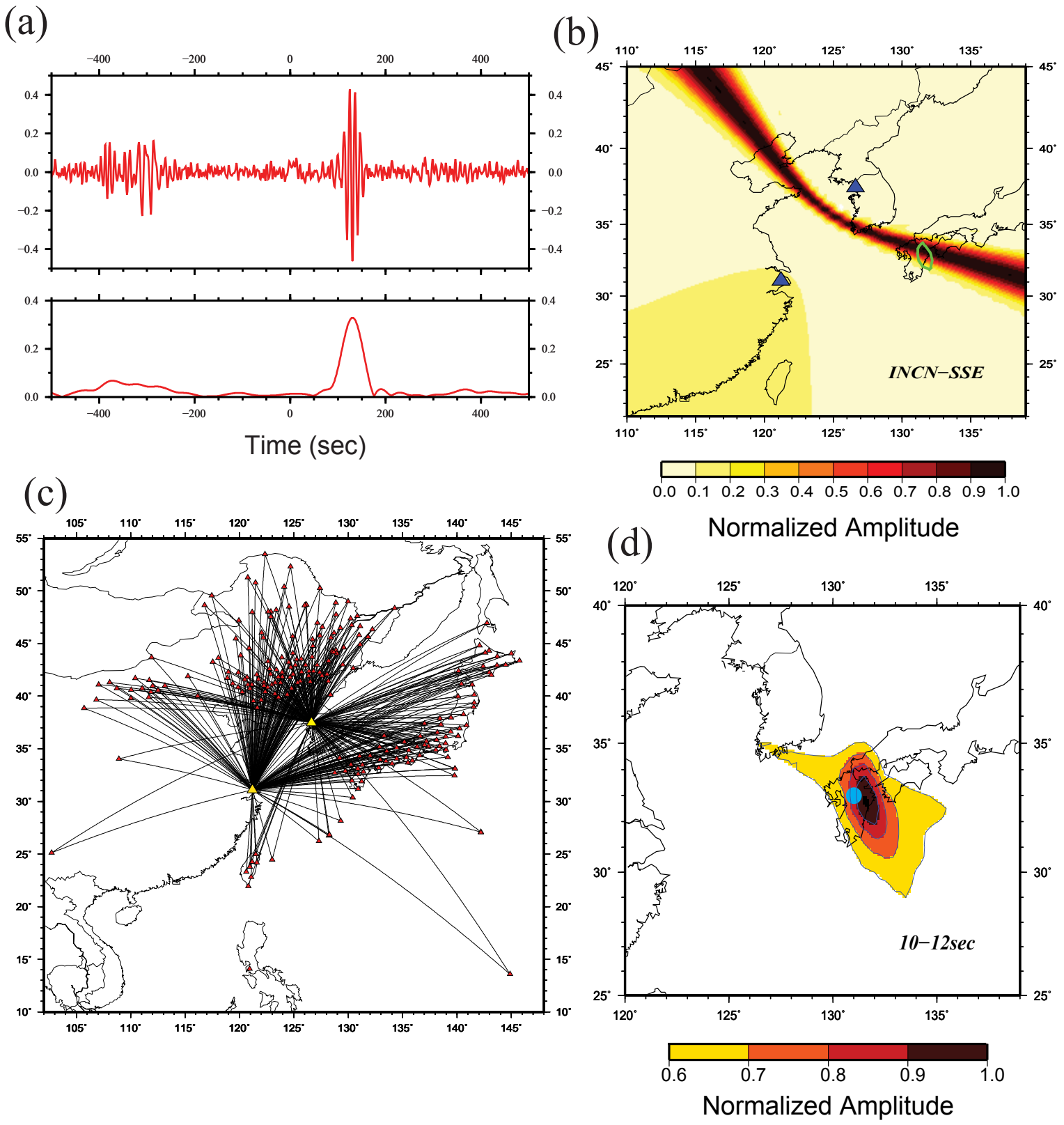
(a)
Time (sec)
(b)
INCN−SSE
Normalized Amplitude
(c)
(d)
10−12sec
Normalized Amplitude

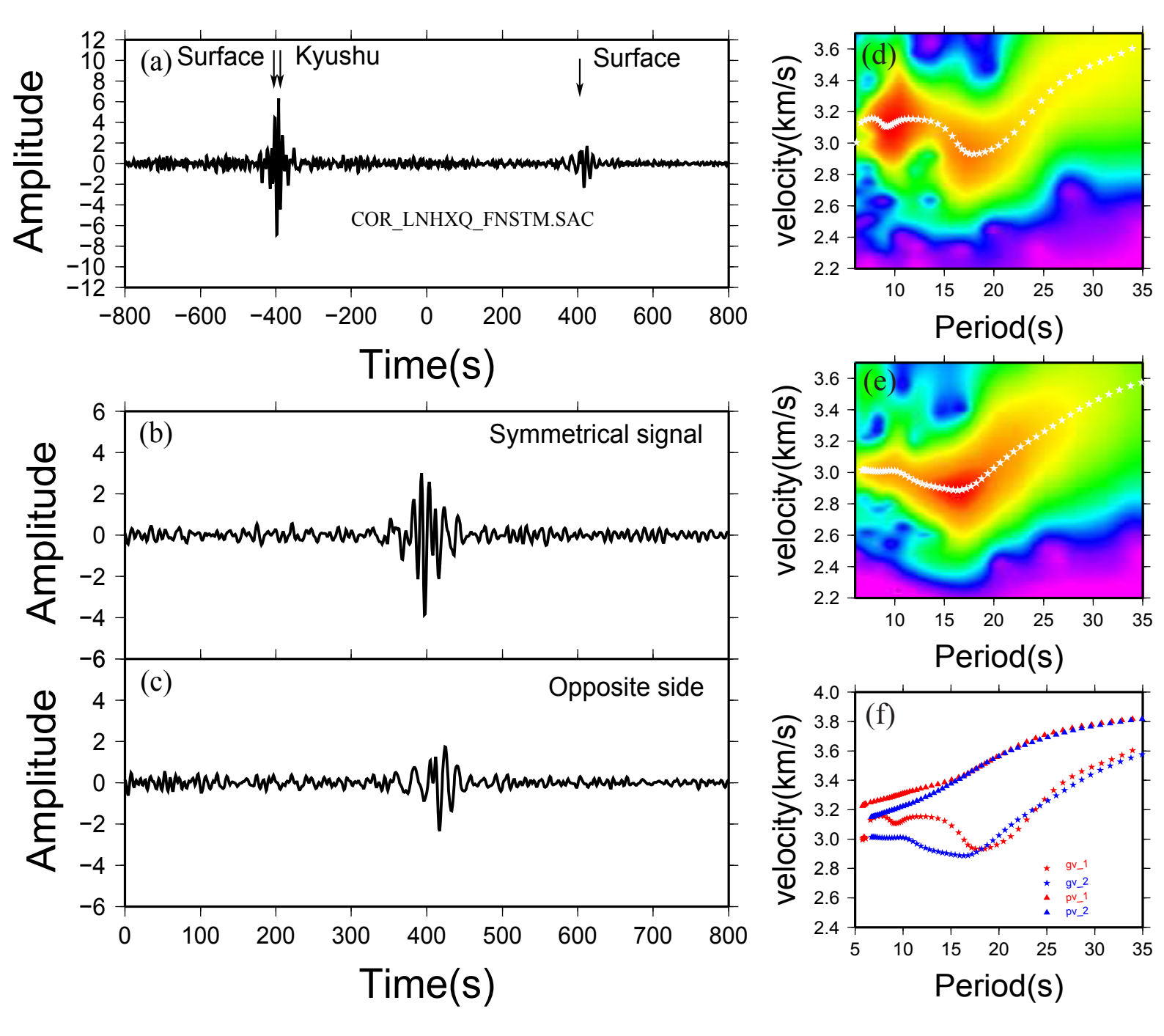
(a)
Surface
Kyushu
Surface
COR_LNHXQ_FNSTM.SAC
Amplitude
Time(s)
(b)
Symmetrical signal
(c)
Opposite side
(d)
(e)
(f)
velocity(km/s)
Period(s)
gv_1
gv_2
pv_1
pv_2

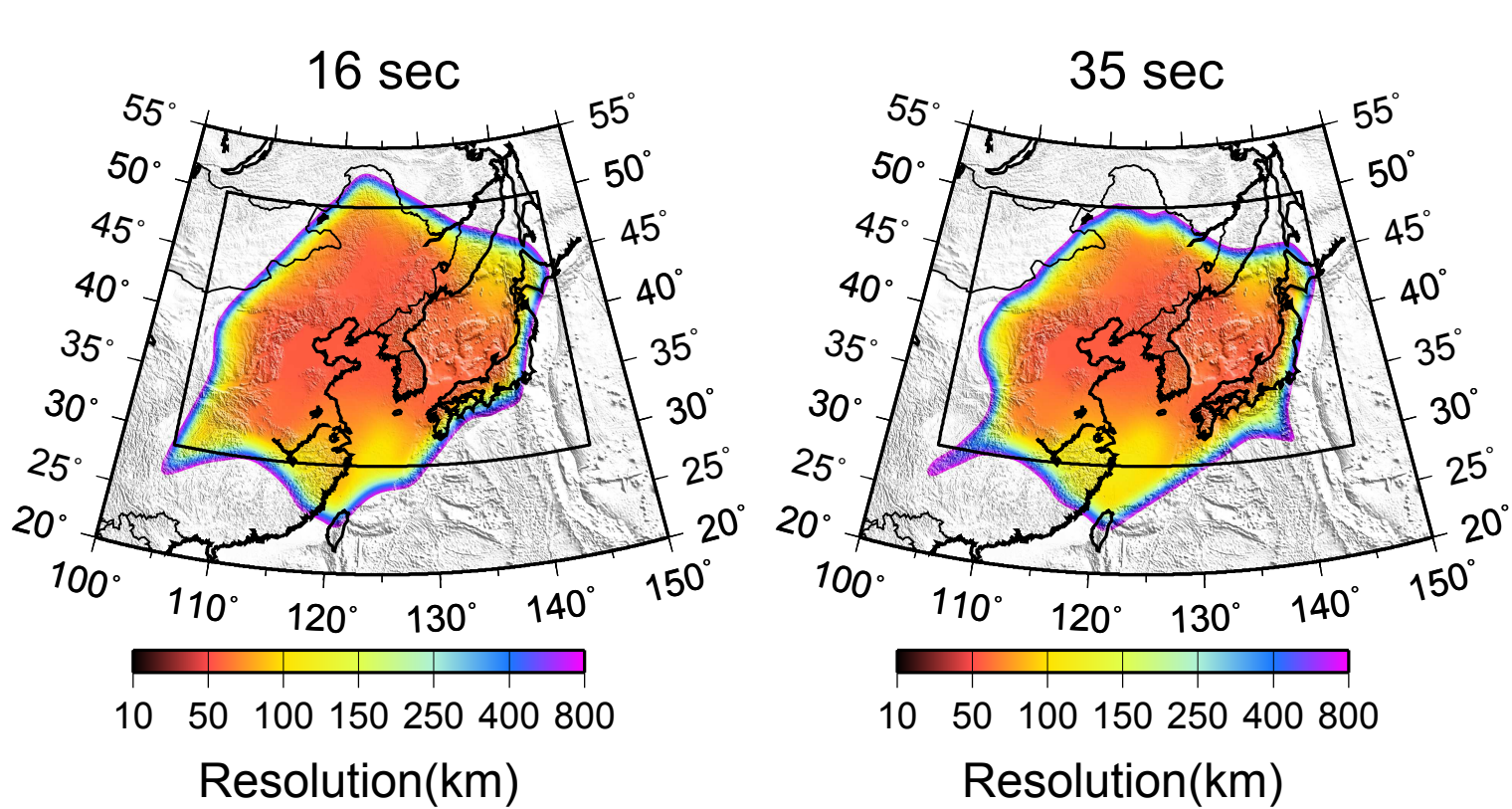
16 sec
35 sec
55°
50°
45°
40°
35°
30°
25°
20°
100°
110°
120°
130°
140°
150°
10 50 100 150 250 400 800
Resolution(km)

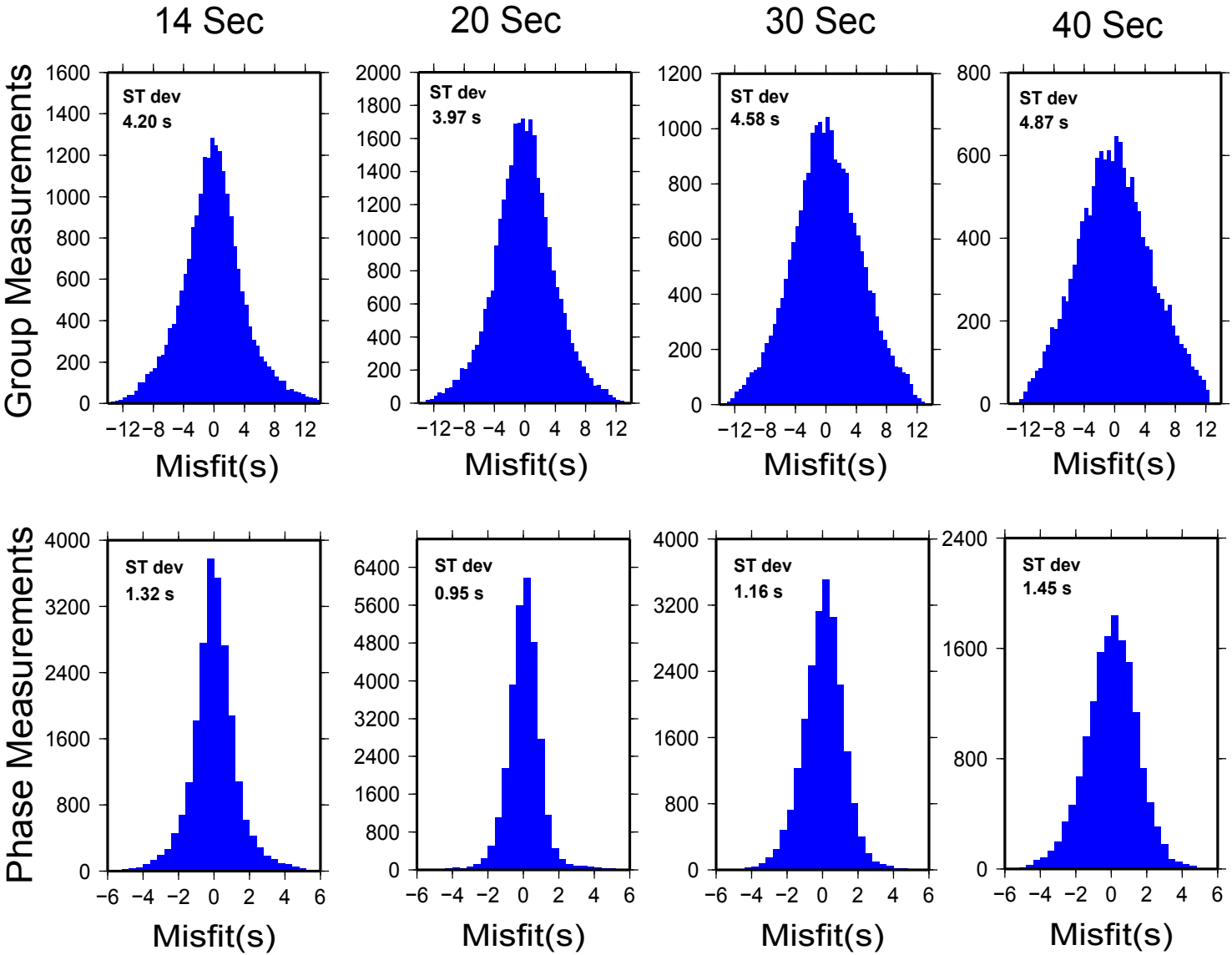
14 Sec
20 Sec
30 Sec
40 Sec
Group Measurements
Phase Measurements
ST dev
4.20 s
ST dev
3.97 s
ST dev
4.58 s
ST dev
4.87 s
ST dev
1.32 s
ST dev
0.95 s
ST dev
1.16 s
ST dev
1.45 s
Misfit(s)

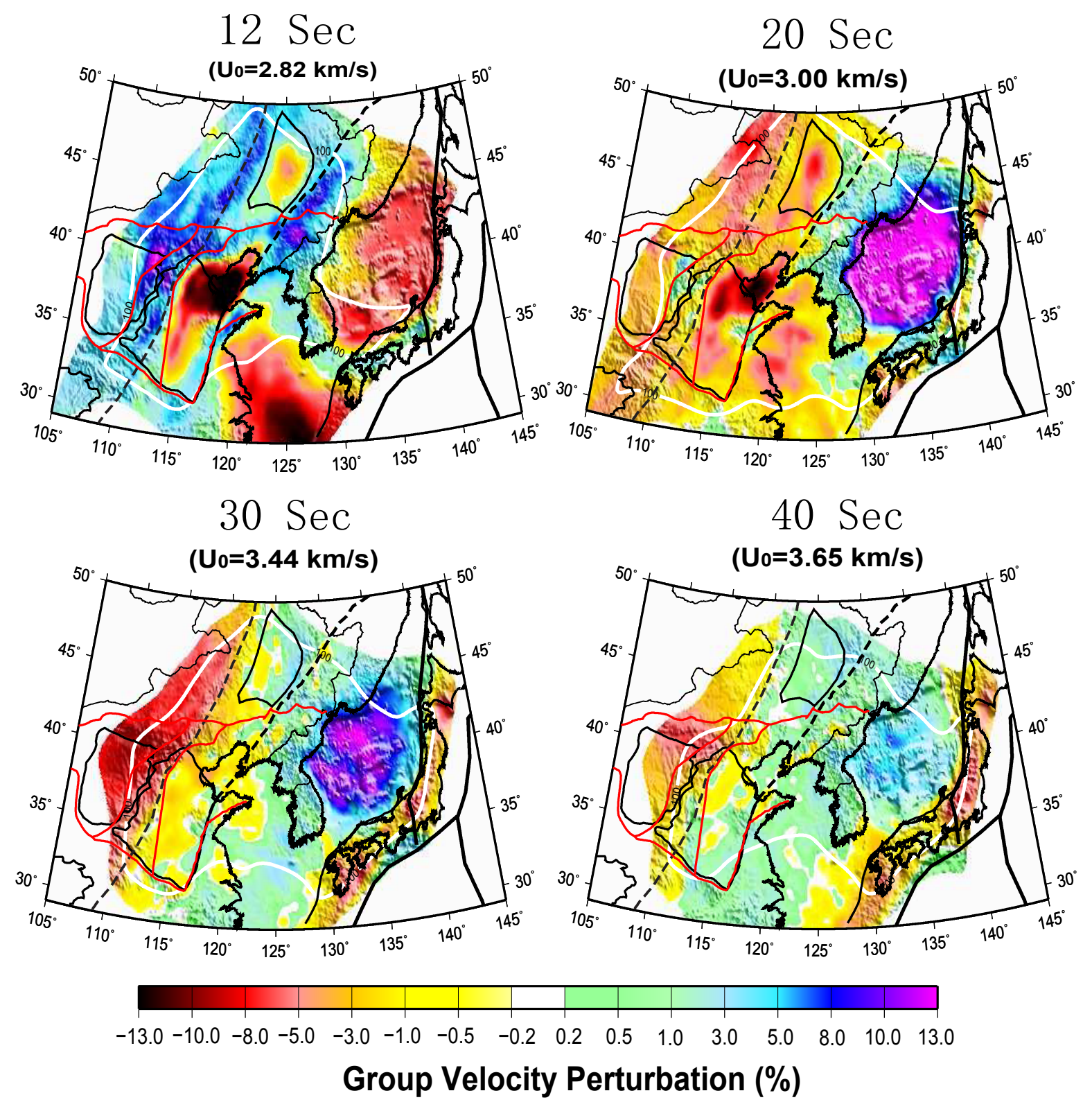
12 Sec
(U0=2.82 km/s)
20 Sec
(U0=3.00 km/s)
30 Sec
(U0=3.44 km/s)
40 Sec
(U0=3.65 km/s)
50°
45°
40°
35°
30°
105°
110°
115°
120°
125°
130°
135°
140°
145°
100
−13.0 −10.0 −8.0 −5.0 −3.0 −1.0 −0.5 −0.2 0.2 0.5 1.0 3.0 5.0 8.0 10.0 13.0
Group Velocity Perturbation (%)

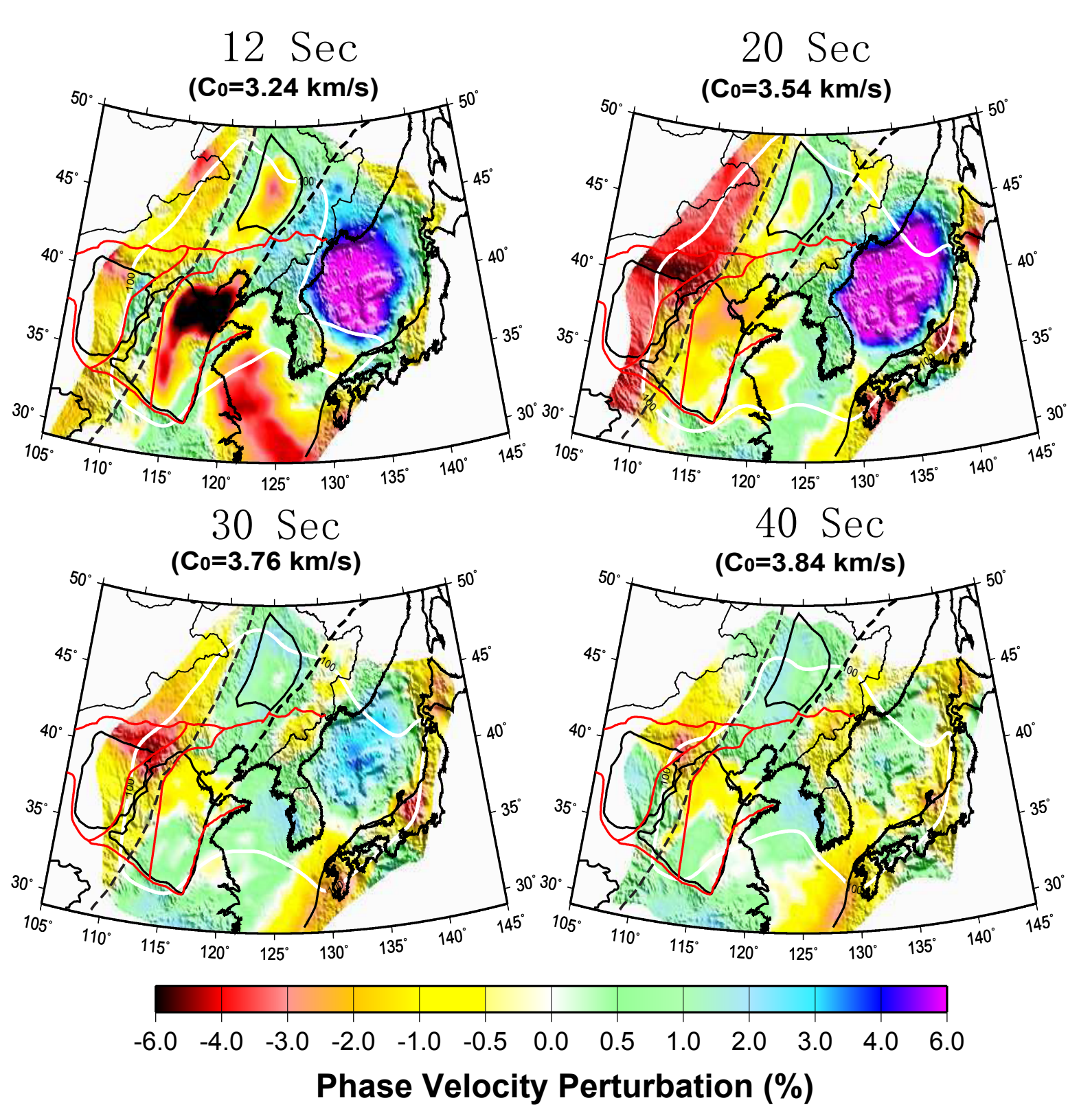
12 Sec
(C0=3.24 km/s)
20 Sec
(C0=3.54 km/s)
30 Sec
(C0=3.76 km/s)
40 Sec
(C0=3.84 km/s)
-6.0 -4.0 -3.0 -2.0 -1.0 -0.5 0.0 0.5 1.0 2.0 3.0 4.0 6.0
Phase Velocity Perturbation (%)

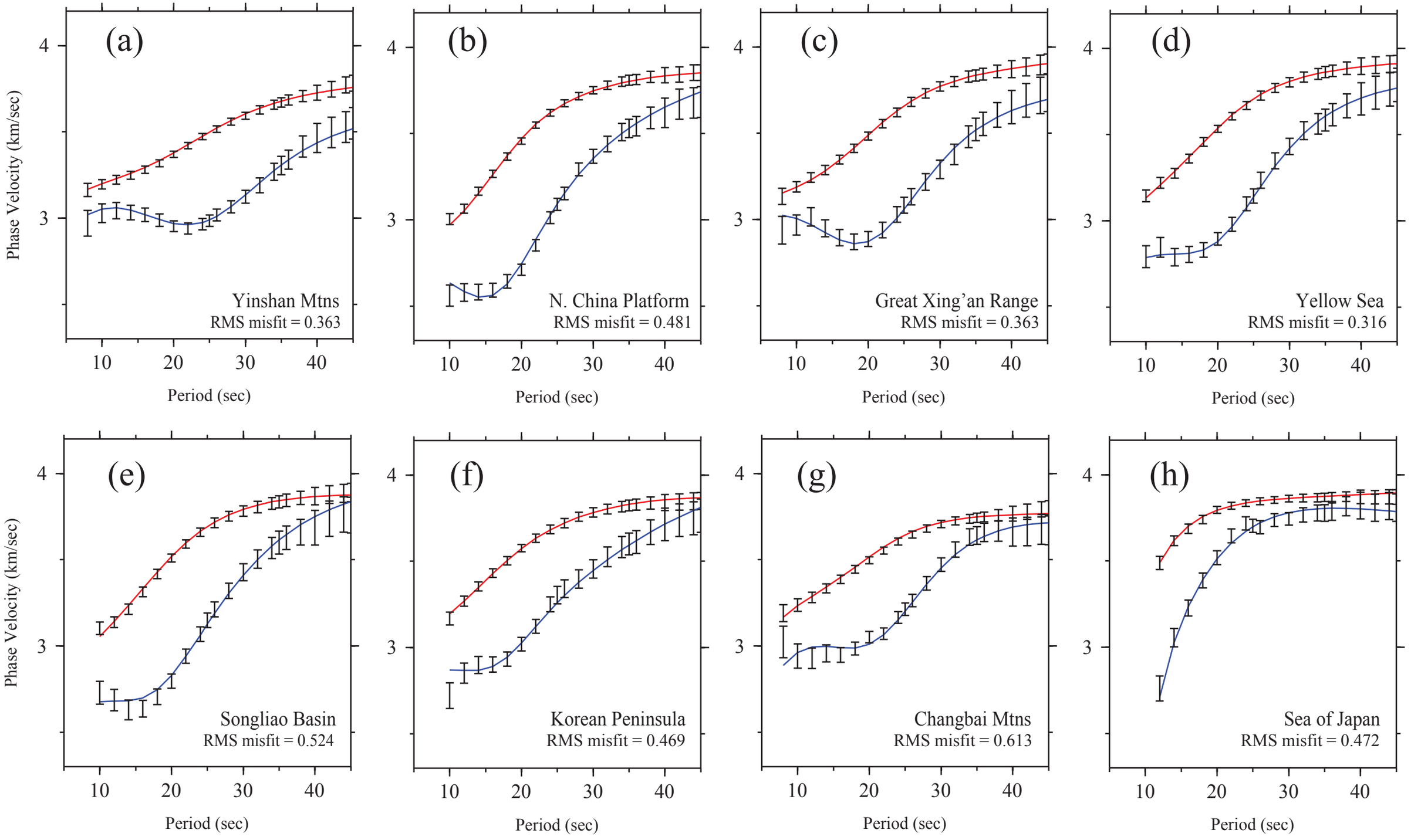
(a)
Yinshan Mtns
RMS misfit = 0.363
(b)
N. China Platform
RMS misfit = 0.481
(c)
Great Xing'an Range
RMS misfit = 0.363
(d)
Yellow Sea
RMS misfit = 0.316
(e)
Songliao Basin
RMS misfit = 0.524
(f)
Korean Peninsula
RMS misfit = 0.469
(g)
Changbai Mtns
RMS misfit = 0.613
(h)
Sea of Japan
RMS misfit = 0.472
Phase Velocity (km/sec)
Period (sec)
3
4
10
20
30
40

(a)
Yinshang Mtns
(b)
N. China Platform
(c)
Great Xing'an Range
(d)
Yellow Sea
(e)
Songliao Basin
(f)
Korean Peninsula
(g)
Changbai Mtns
(h)
Sea of Japan
Depth (km)
Vsv (km/sec)
0
10
20
30
40
50
60
70
80
90
100
3
4
5

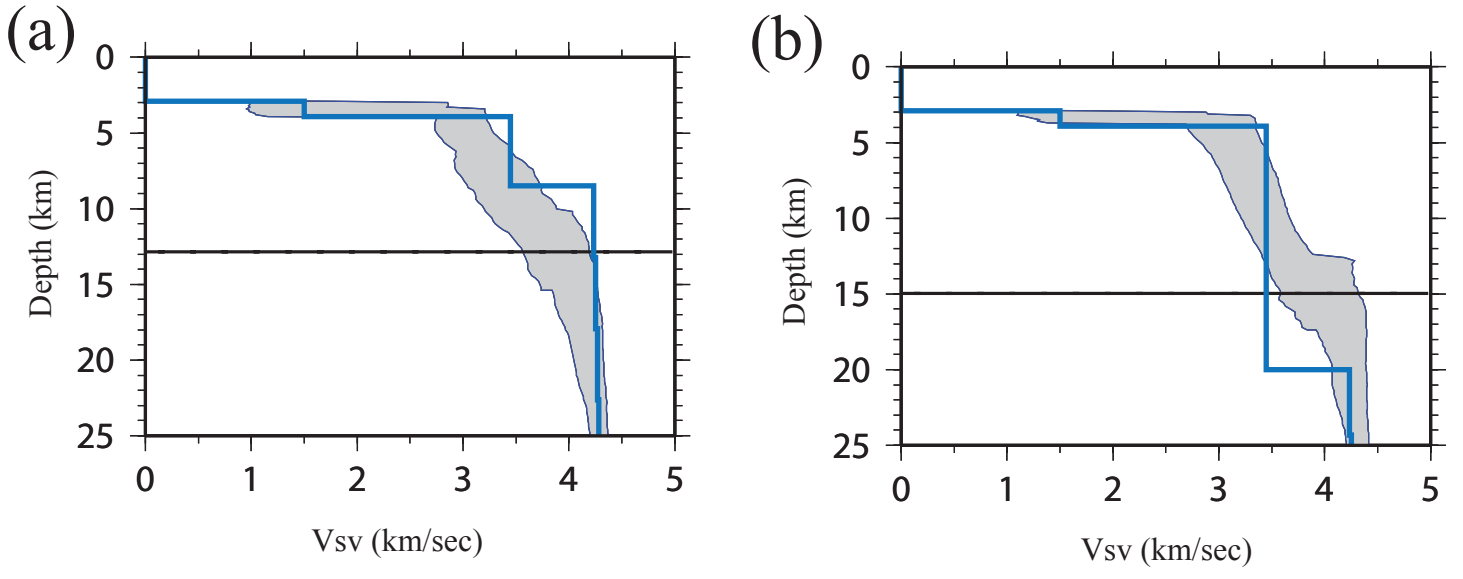
(a)
Depth (km)
0
5
10
15
20
25
0
1
2
3
4
5
Vsv (km/sec)
(b)
Depth (km)
0
5
10
15
20
25
0
1
2
3
4
5
Vsv (km/sec)

(a) Lower Crust

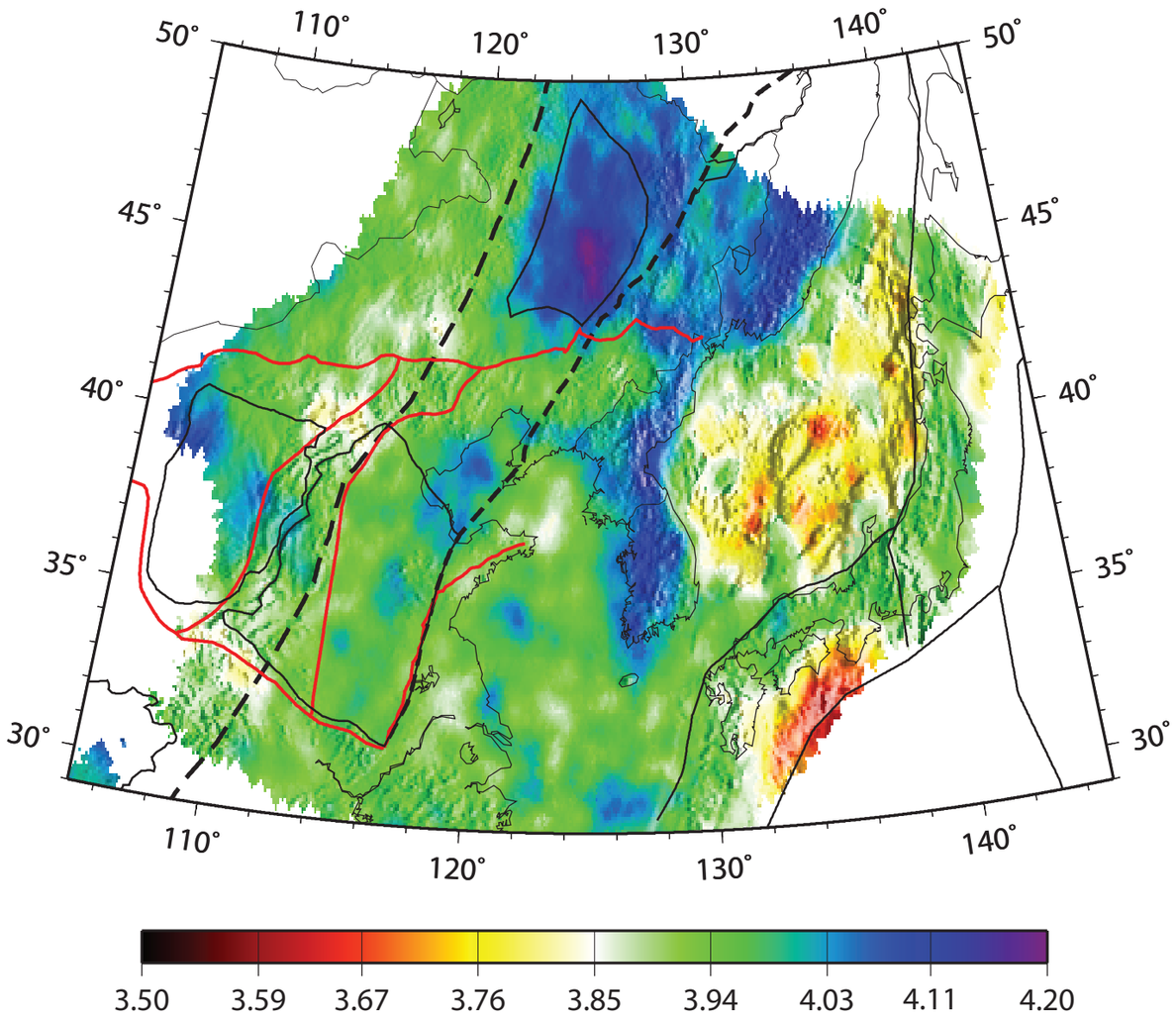

(b) Depth = 40 km

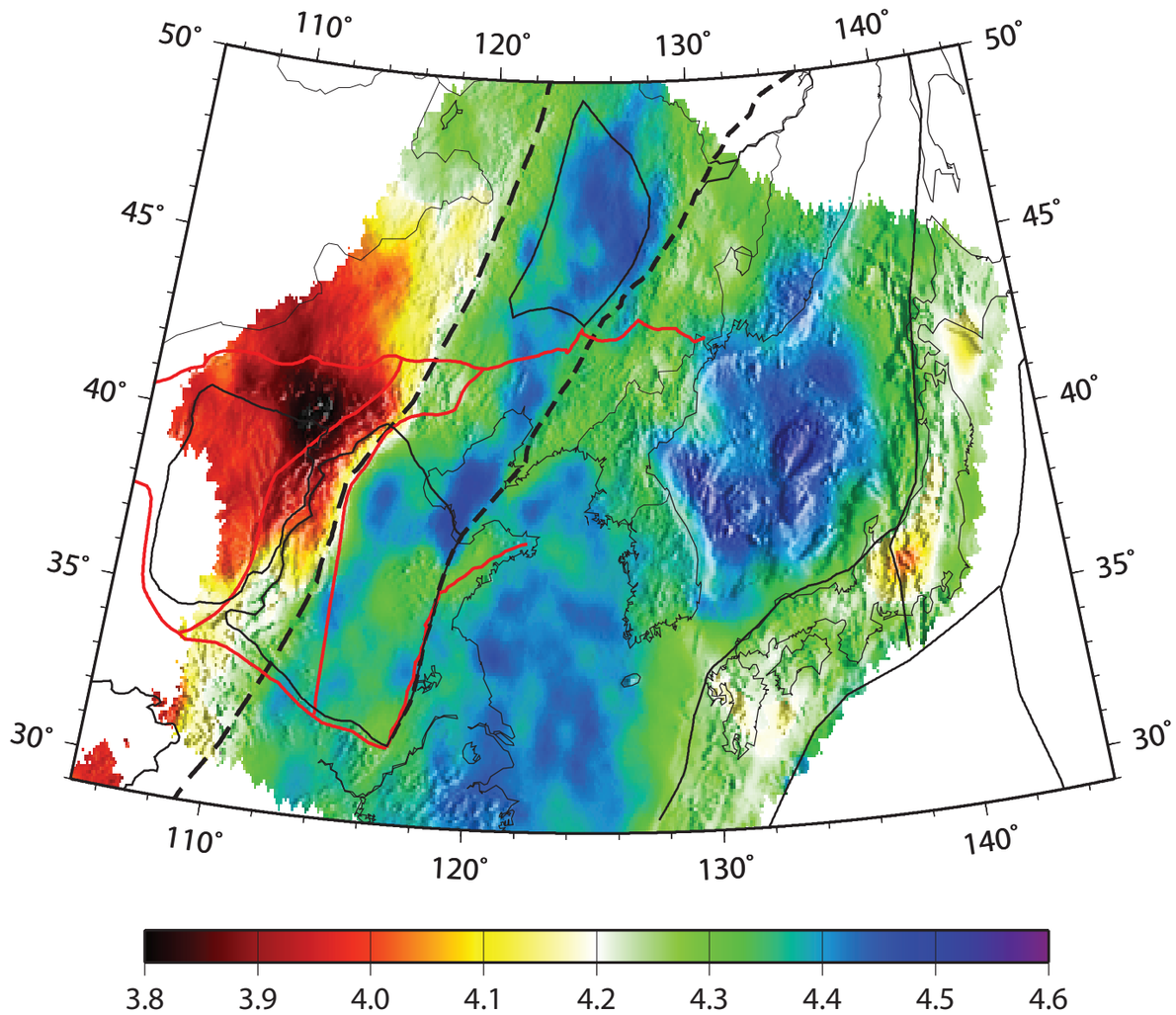

(c) Depth = 60 km

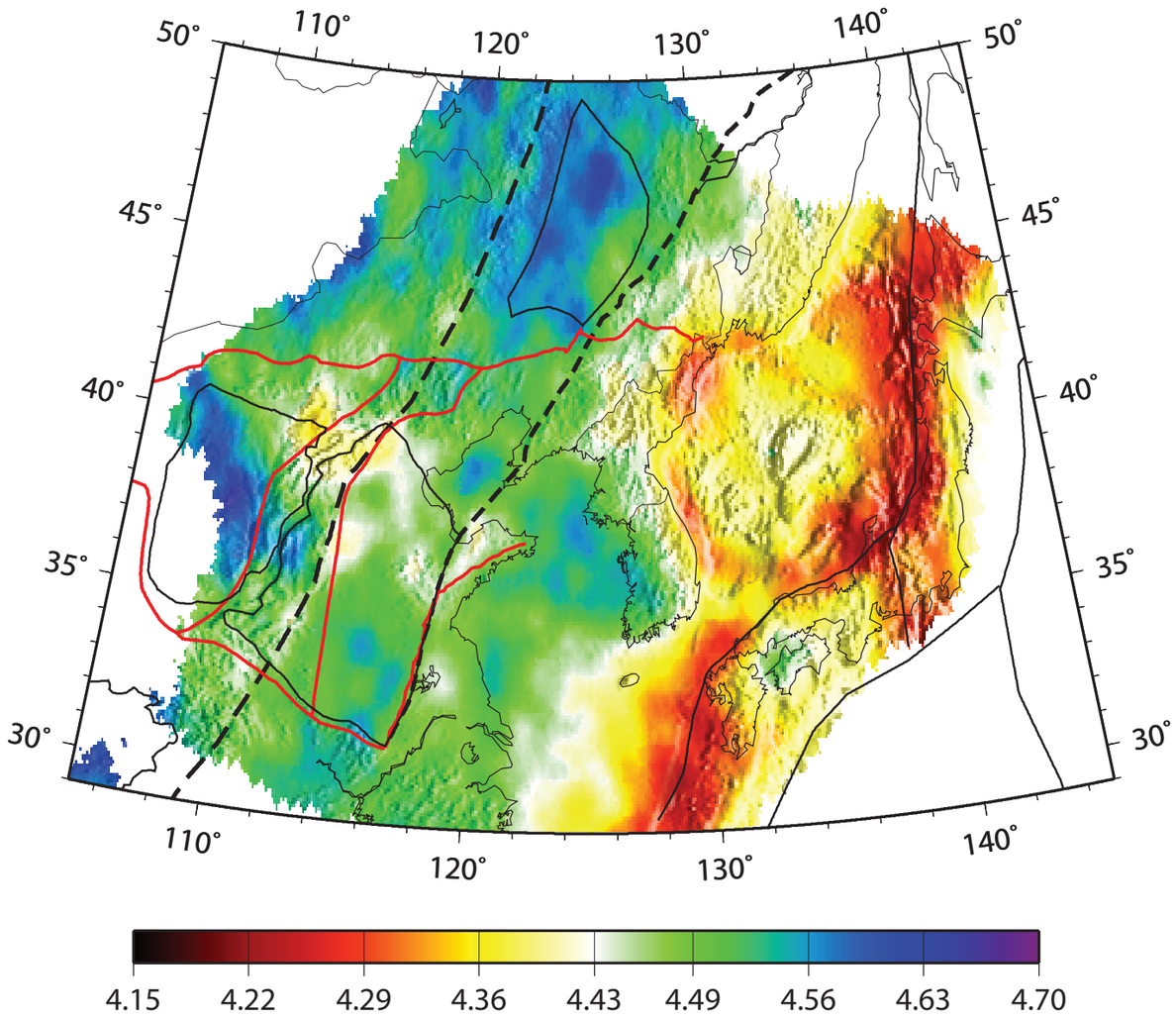

(d) Depth = 80 km

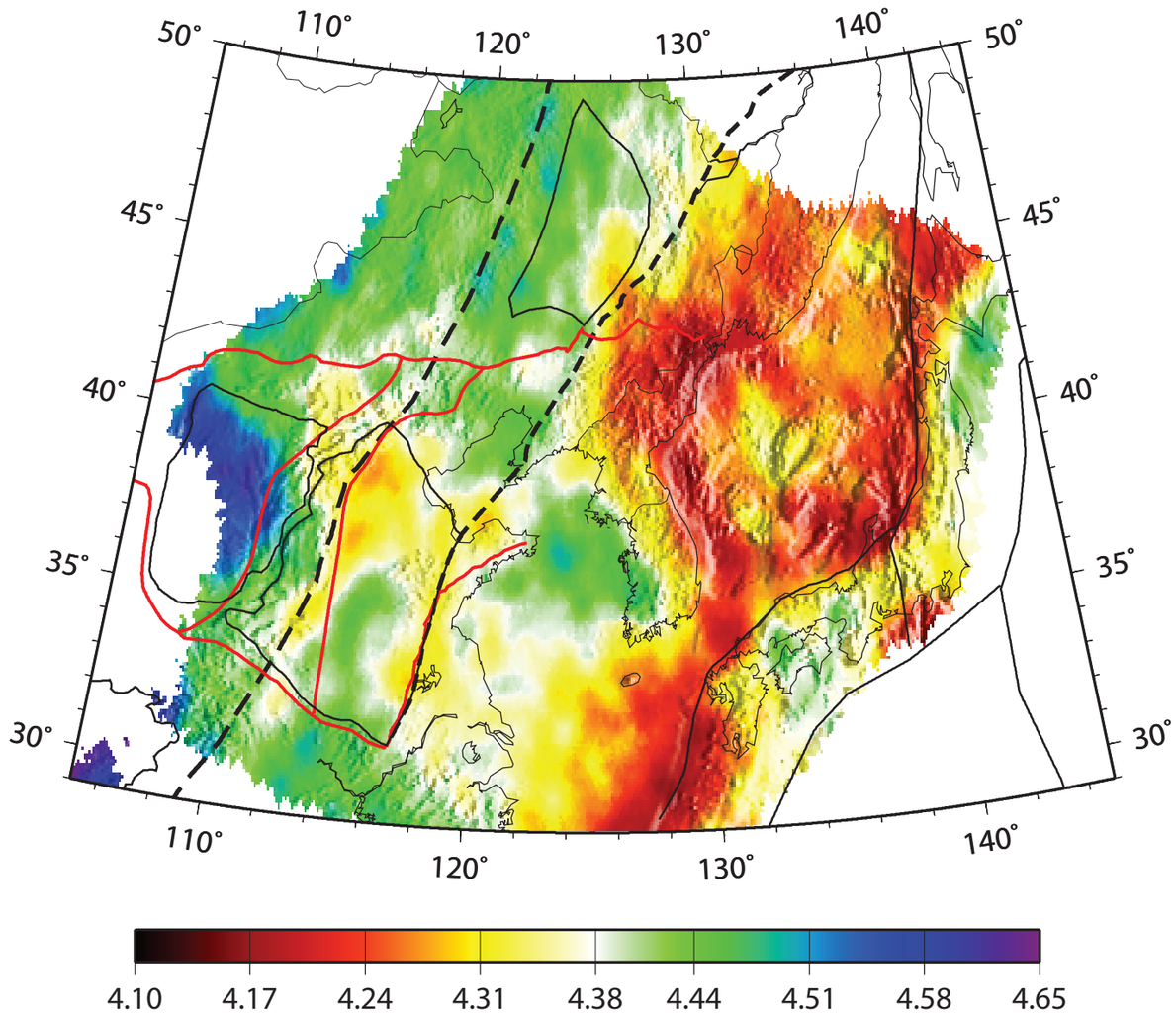

(a) Crustal Thickness (km)

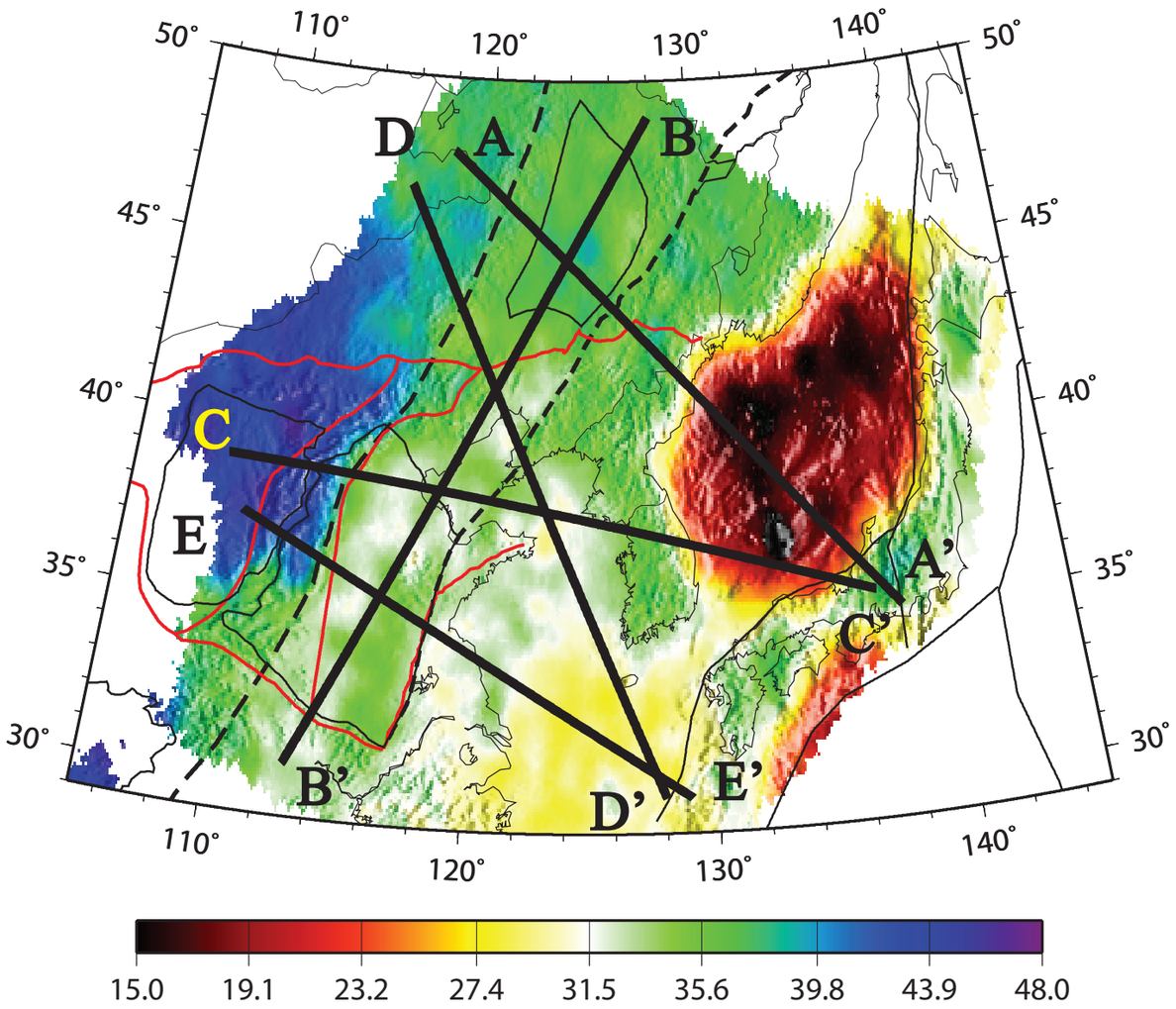

15.0 19.1 23.2 27.4 31.5 35.6 39.8 43.9 48.0

(c) Velocity Jump (km/sec)

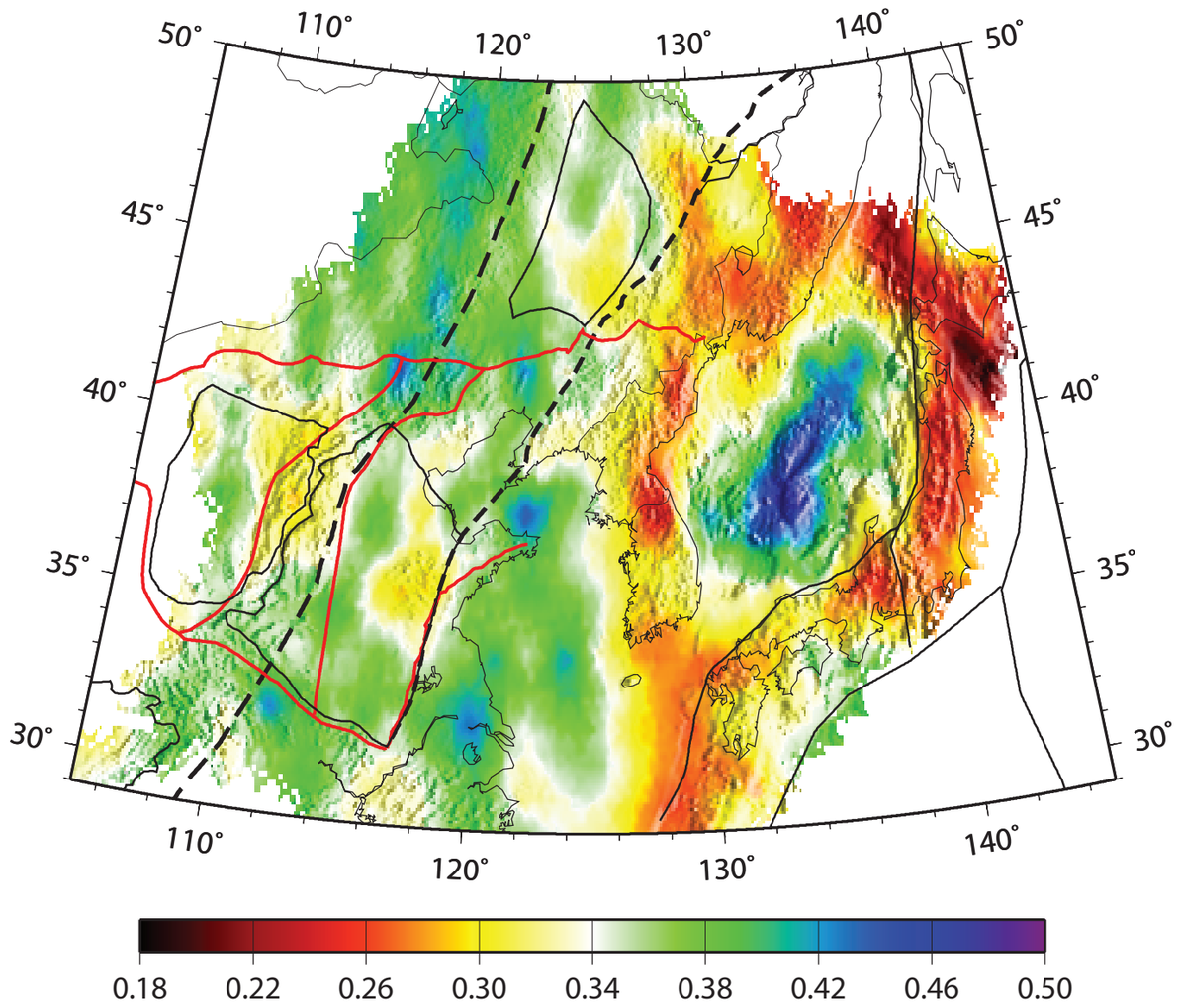

0.18 0.22 0.26 0.30 0.34 0.38 0.42 0.46 0.50

(b) Uncertainties (km)

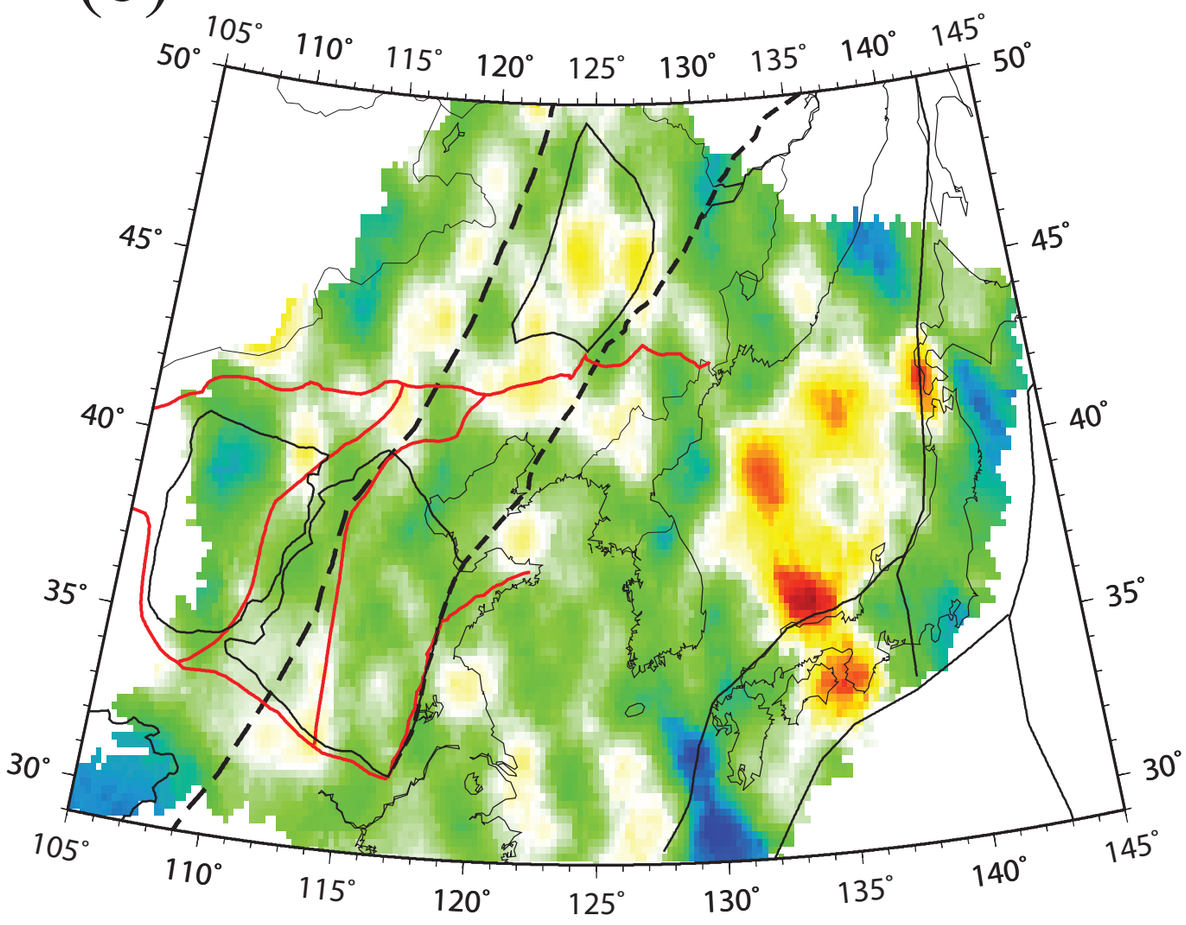

1.50 1.94 2.38 2.81 3.25 3.69 4.12 4.56 5.00

(d) Uncertainties (km/sec)

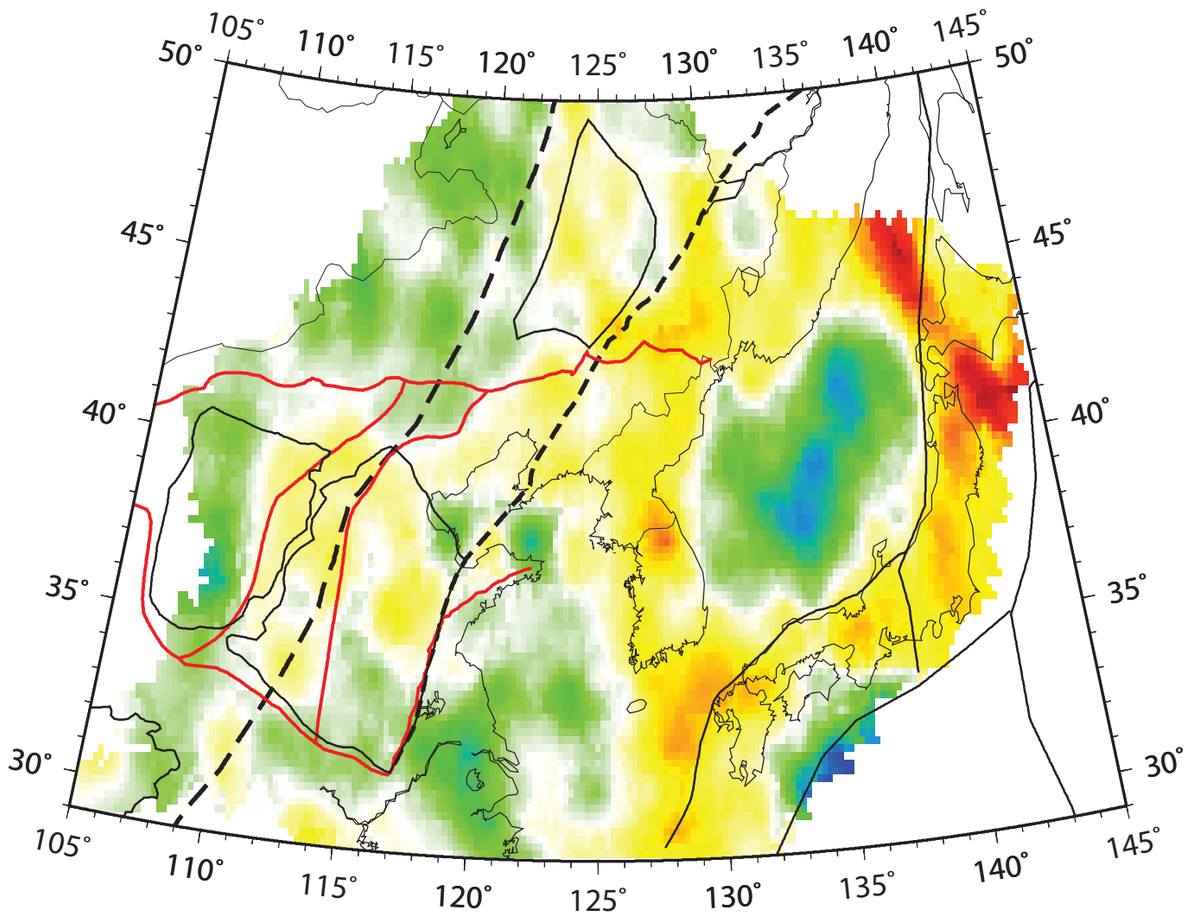

0.050 0.075 0.100 0.125 0.150 0.175 0.200 0.225 0.250

(a) Lower Crust

(b) Depth = 40km

(c) Depth = 60km

(d) Depth = 80km

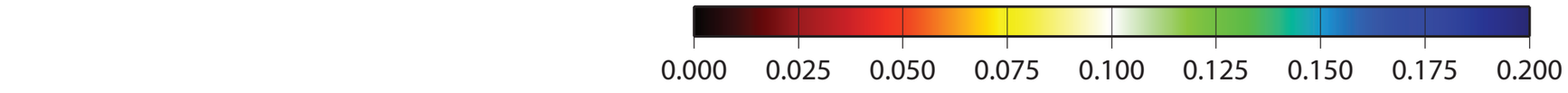

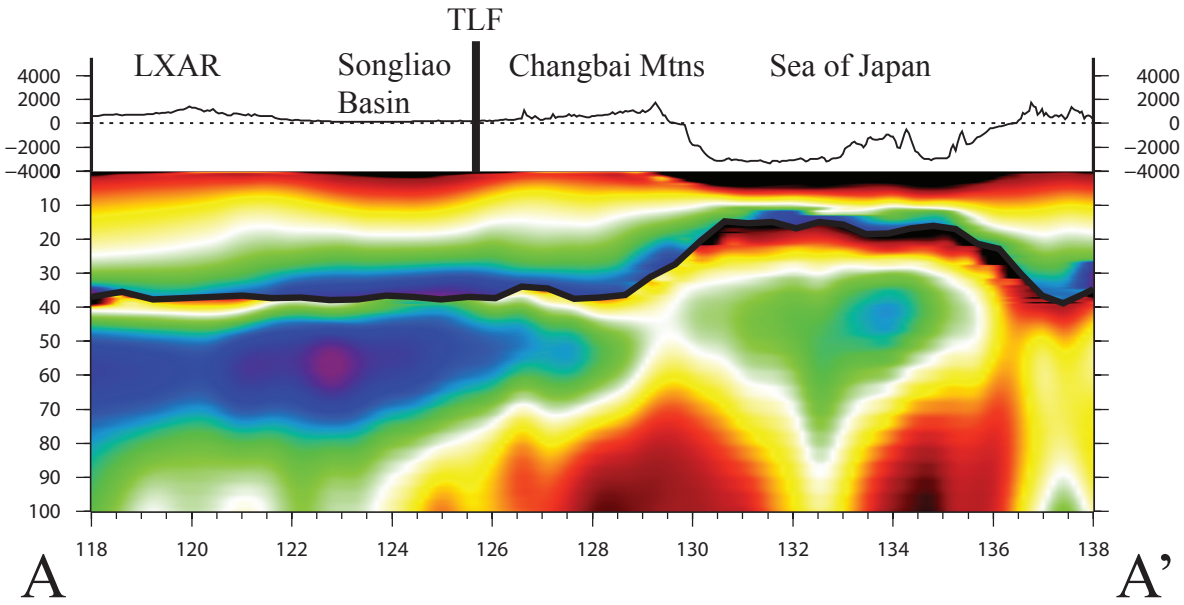
TLF
LXAR
Songliao Basin
Changbai Mtns
Sea of Japan
4000
2000
0
−2000
−4000
10
20
30
40
50
60
70
80
90
100
118
120
122
124
126
128
130
132
134
136
138
A
A’

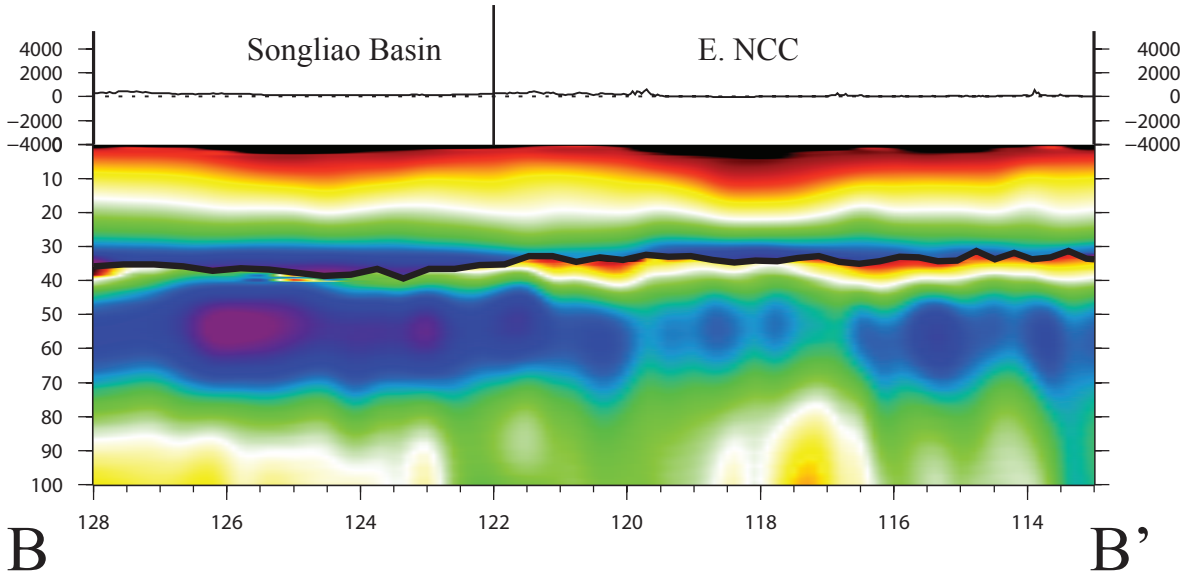
Songliao Basin
E. NCC
4000
2000
0
−2000
−4000
10
20
30
40
50
60
70
80
90
100
128
126
124
122
120
118
116
114
B
B’

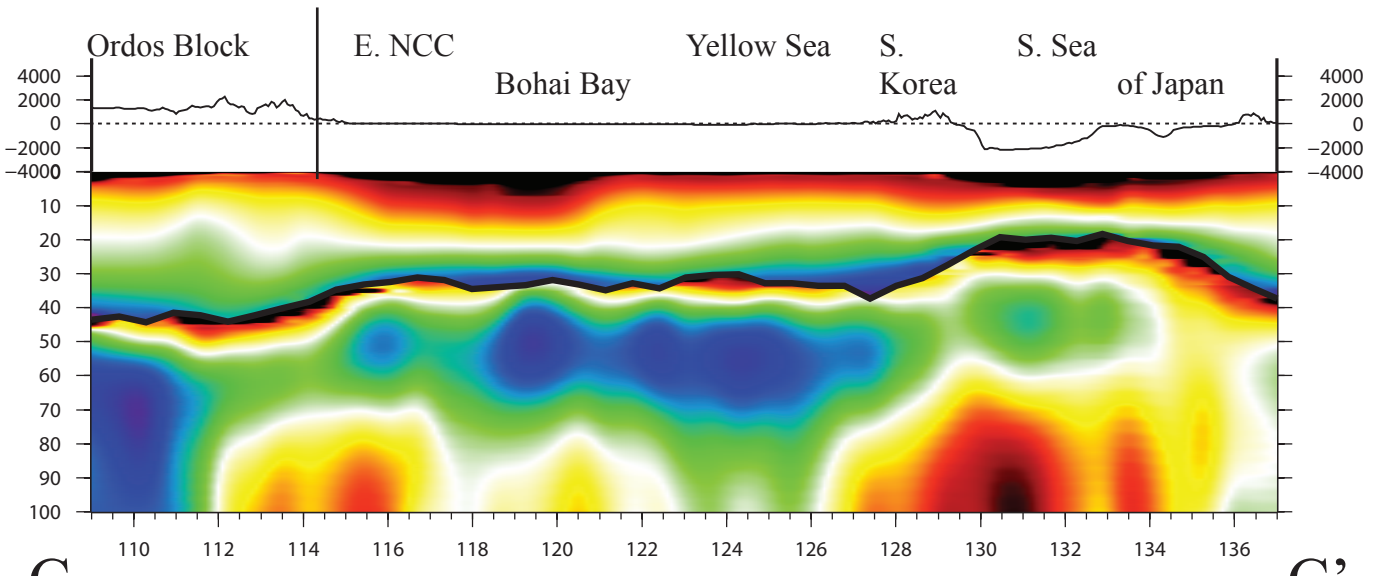
Ordos Block
E. NCC
Bohai Bay
Yellow Sea
S. Korea
S. Sea of Japan
4000
2000
0
−2000
−4000
10
20
30
40
50
60
70
80
90
100
110
112
114
116
118
120
122
124
126
128
130
132
134
136
C
C’

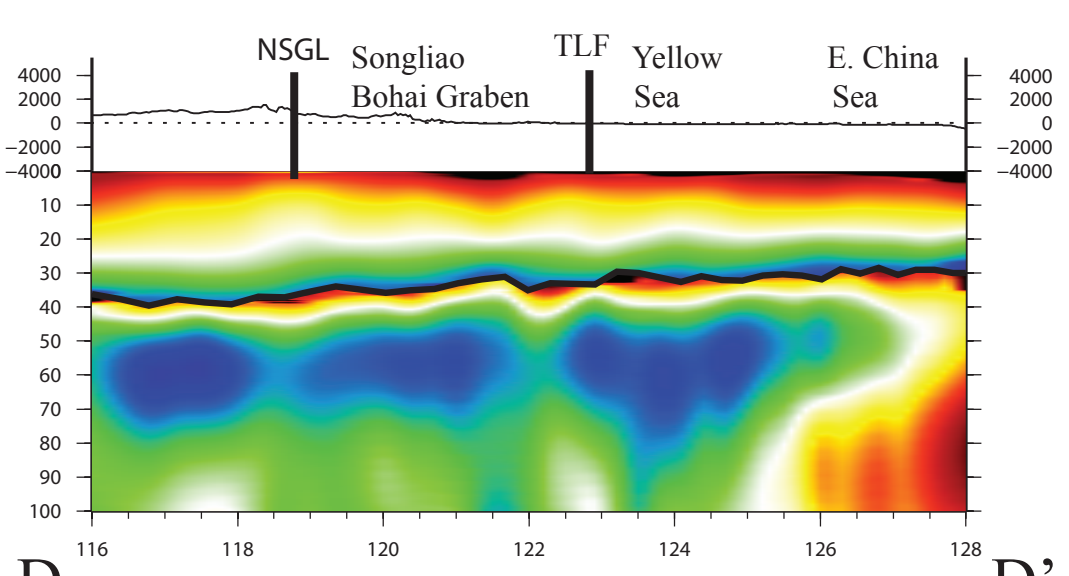
NSGL
Songliao Bohai Graben
TLF
Yellow Sea
E. China Sea
4000
2000
0
−2000
−4000
10
20
30
40
50
60
70
80
90
100
116
118
120
122
124
126
128
D
D’

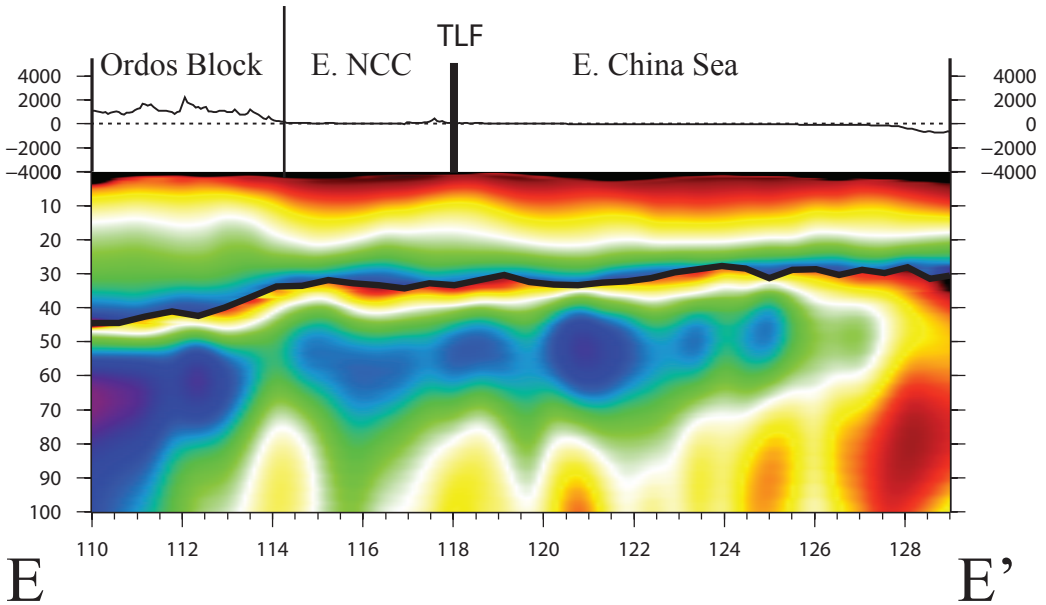
Ordos Block
E. NCC
TLF
E. China Sea
4000
2000
0
−2000
−4000
10
20
30
40
50
60
70
80
90
100
110
112
114
116
118
120
122
124
126
128
E
E’

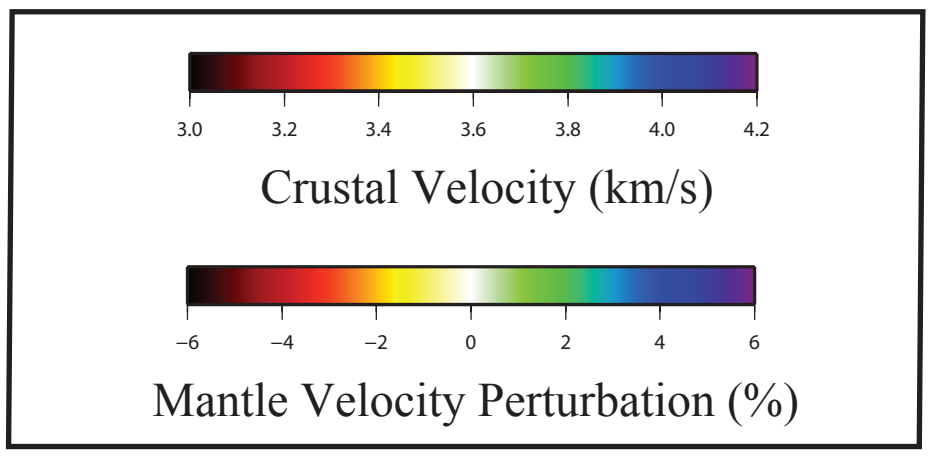
3.0
3.2
3.4
3.6
3.8
4.0
4.2
Crustal Velocity (km/s)
−6
−4
−2
0
2
4
6
Mantle Velocity Perturbation (%)

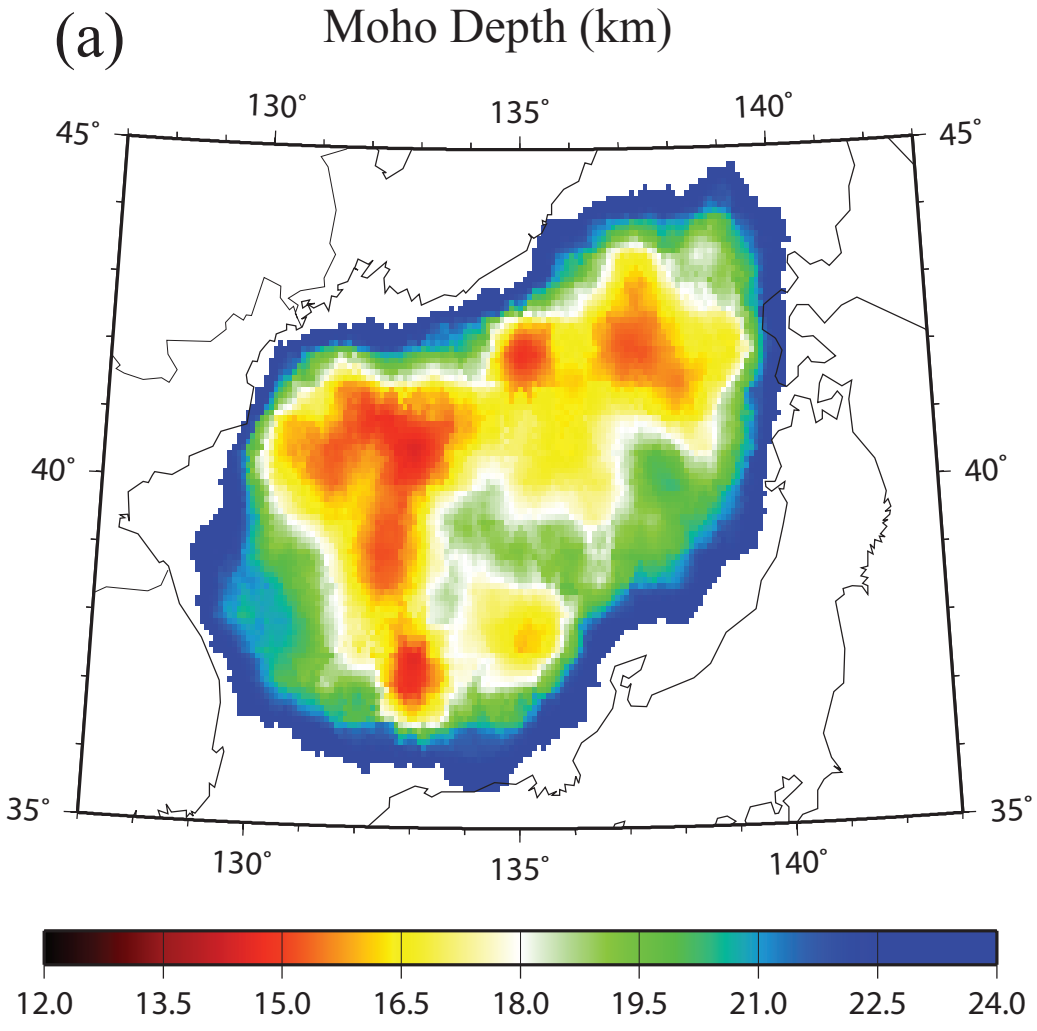
(a)
Moho Depth (km)
130°
135°
140°
45°
40°
35°
12.0
13.5
15.0
16.5
18.0
19.5
21.0
22.5
24.0

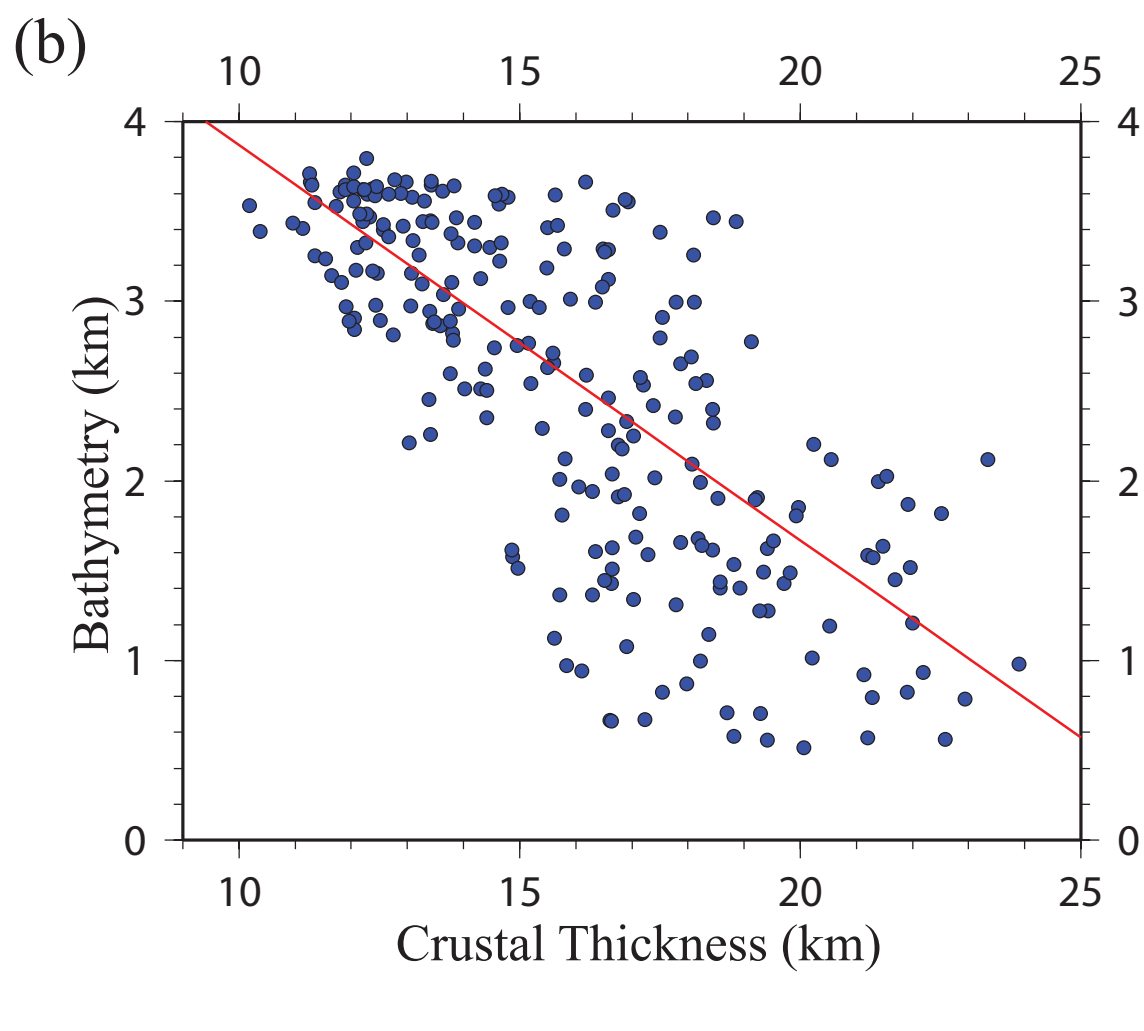
(b)
Bathymetry (km)
Crustal Thickness (km)
10
15
20
25
0
1
2
3
4

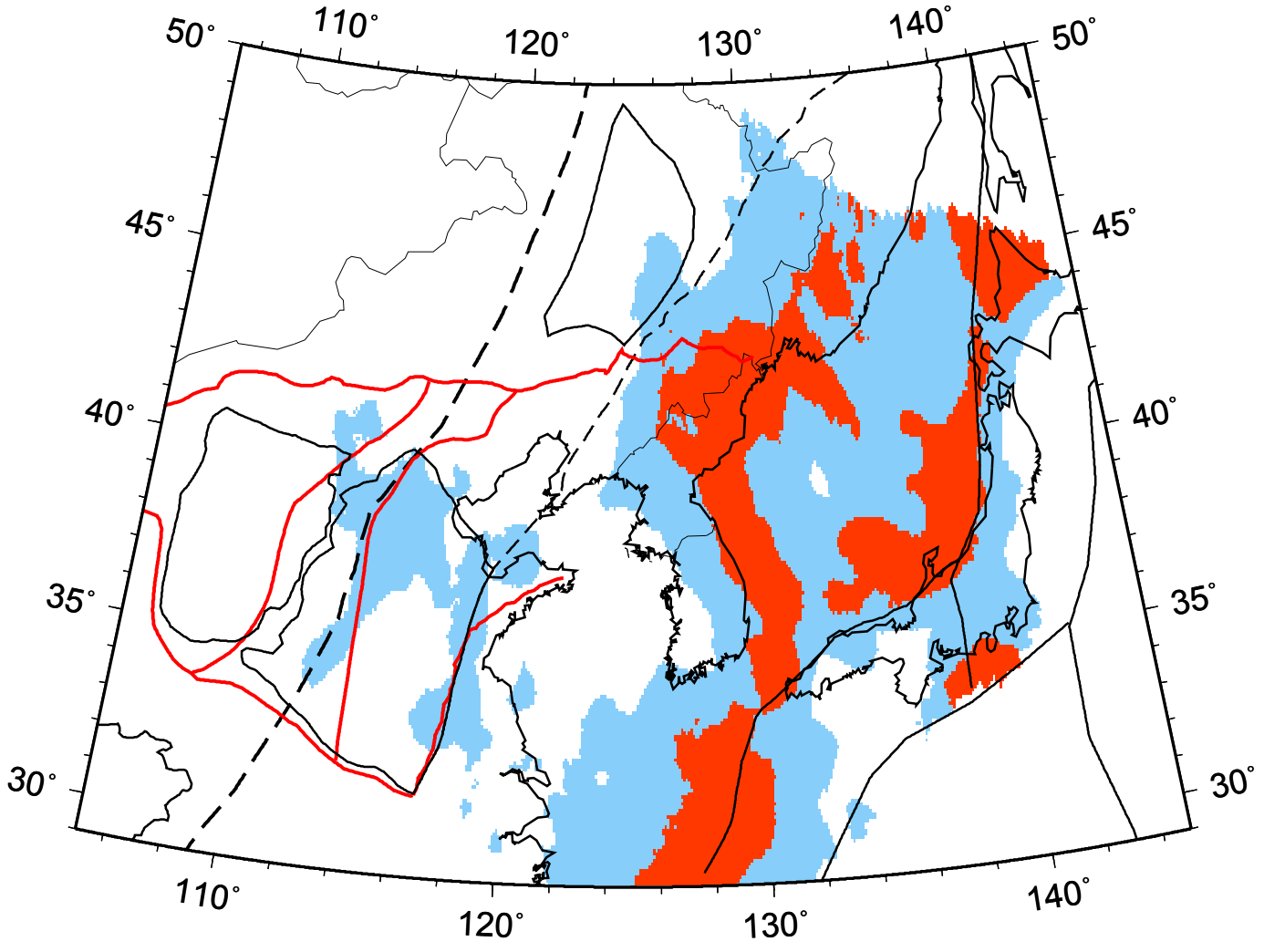
50°
110°
120°
130°
140°
50°
45°
45°
40°
40°
35°
35°
30°
30°
110°
120°
130°
140°